III-V Semiconductor Nanowires
growth and characterisation

Giulio Ungaretti
Master’s Thesis
August 2014

Supervisors:
Jesper Nygård &
Peter Krogstrup

Copenhagen University

``Entropy is the price of structure.''
Ilya Prigogine
Order Out of Chaos: Man's New Dialogue with Nature

Abstract

Semiconductor nanowires, tiny and marvelous materials, have been object of intense research in the past few decades for their unique properties and possible applications. From the first successful synthesis and understanding of their growth mechanism an ever growing amount of fundamental knowledge has been obtained in epitaxial growth. Furthermore their properties have been exploited to study fundamental problems in solid state physics, such as quantum transport and light confinement. Also, nanowires have shown the potential to be the building blocks of future technologies, fulfilling the need of continuous miniaturization. Yet, a complete understanding of the growth dynamics enabling a precise control of shape, size and composition has not been reached.

This thesis reports on the fabrication of substrates for nanowire growth and X-ray studies on the dynamics of nanowire growth both, topics being crucial for the fundamental understating of the mechanism of the epitaxial growth of nanowires.

We present the fabrication process of indium arsenide substrates that allows to control the size and the position of nanowires along with the first steps to obtain nanowire networks. Moreover we show a novel family of indium arsenide substrates with a thin film of silicon dioxide.

By studying the growth dynamics we find out that it is possible to create abrupt crystal phase changes by solid phase reconstruction transitions in gold assisted indium arsenide nanowires grown with molecular beam epitaxy (MBE). We also determine the incubation time for MBE gold assisted indium arsenide nanowire growth and we show how in-situ X-ray studies can give more informations on the growth dynamics of nanowires.

Contents

Thesis Outline

This thesis address two main topics: the preparation of substrates for nanowire growth and studies on the dynamics of nanowire growth.

The dynamics of nanowire growth are first introduced in chapter **Chapter 1**, where thermodynamic and kinetic models of nanowire growth are presented. X-ray diffraction is the technique-of-choice to study growth dynamics, and the basics are also introduced in **Chapter 1**, along with an introduction to nanowires' crystal structures. Lastly, a general description of molecular beam epitaxy is presented.

Chapter 2 is focused on the substrate's business. The fabrication process is explained focusing on the troublesome steps. The complete set of recipes is instead given in the appendices. The advances in substrate fabrication for nanowire networks are reported in 2.3.1.
Lastly the salient results for the fabrication and growth on the novel SiO_2-InAs family substrates are reported in 2.3.2.

Chapter 3 presents the in-situ X-ray measurement performed at the SPring8 synchrotron in Hyogo, Japan. The experiments address the dynamics of Au-catalyzed InAs nanowires by the means of time resolved in-situ X-ray diffraction.

During this project I performed all the substrate fabrication and characterization, whereas the actual growth of the wires was performed by Peter Krogstrup; I was often responsible for other MBE tasks such as substrates loading and degassing. The X-ray experiments are performed together with Peter Krogstrup and Tomas Stankevic, PhD fellow at the Neutron and X-Ray Scattering group at NBI.

1 | Introduction

Nanomaterials are a broad class of materials whose properties are strongly influenced by size effects. In general size effect play a significant role when one dimension of the material is in the range going from few nanometers (10^{-9}m) and reaching up to hundreds of nanometers. Size effects include changes in the strength of the material, electronic and optical properties and more. Some of the most notable nanomaterials are quantum dots, nanowires, carbon nanotubes and graphene, just to name a few. Not only these materials are interesting for their possible applications but also because they are good platforms to perform fundamental studies on any of the aforementioned size effects. Moreover most nanomaterials offer a degree of tunability in their shape, size and composition and thus in their properties that is unmatched by any other material class, but a the same time poses the one of the biggest challenges, namely, the ability to have a precise control of these characteristics.

In this chapter I will introduce a specific class of nanomaterials, semiconductor nanowires, describe the basics of epitaxial growth via molecular beam epitaxy, explain their crystal structure and how to index relevant directions and planes and introduce some of the basics concepts of X-ray diffraction required to understand the experiments presented in this thesis. Lastly I will introduce the theoretical formalism to describe growth kinetics.

1.1 Semiconductor Nanowires

Nanowires are what I would call, maybe shamelessly, a class of wonder-materials. The reasons for such a bold statement are many some of which I shall explain in this thesis and the remainders can be easily glanced upon with a simple query of Google Scholar or Web Of Science. Most of the peculiar properties are consequences of their quasi one dimensional nature.

Semiconductor nanowires are nanosized object with an outer shape resembling that of a wire, a long and thin object. Usual dimension for semiconductor NWs are in the range of tens to hundreds of nm for their width and microns for their length. The morphology of the wires strongly depends on their composition and crystal structure. As an example a scanning electron microscope (SEM) micrograph of an InAs nanowire, showing an hexagonal morphology with clearly defined facets is reported in figure 1.1. Nanowires are said to grow epitaxially, meaning that their crystal orientation has a well-defined relation with the substrate upon which they grow. All the nanowires presented in this thesis are Au-assisted InAs grown by solid source molecular beam epitaxy (MBE), using the vapor liquid solid mechanism (VLS). The VLS mechanism uses catalytic liquid alloy droplets that can rapidly reach supersaturation and act as nucleation centers from which crystal growth can start.

The nanowires presented in this thesis are grown either with a Varian GEN II machine at Niels Bohr Institute in Copenhagen (NBI) or with a custom system attached to X-ray diffractometer at the BL11XU beam-line,SPring8 synchrotron. Before proceeding any further with the description of their crystal structure and introducing the model of nanowire growth, it is worth spending a few words on the general principles of molecular beam epitaxy.

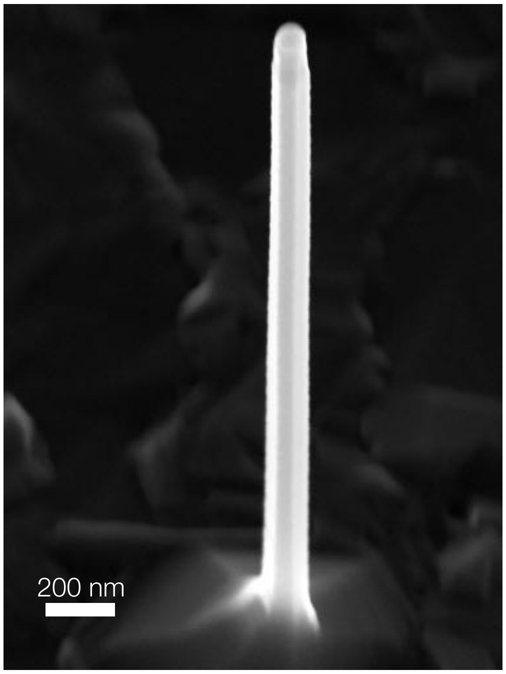

Figure 1.1: Scanning electron microscope micrograph of an InAs nanowire growing on top of an InAs substrate. The nanowire shows six clear facets, three of which are visible in the micrograph and has a hexagonal cross-section.

1.1.1 Molecular Beam Epitaxy

Molecular beam epitaxy is an ultra high vacuum (UHV) technique where beams of ultra pure solid state materials are generated in so called effusion cells by evaporating or sublimating high purity materials in radiatively heated and thermally insulated (to prevent cross talks) crucibles. The crucible's aperture ensures the creation of a collimated atomic beam, and the UHV guarantees a very long mean free path (approximately $10^6 m$ at 10^{-10} torr). UHV condition is obtained by a series of pumps. The setup depends on the specific machine but a usual set-up consist of one or two cryo-pumps coupled with a ion-sublimation-pump, lastly a liquid nitrogen cooled cryo-shied surrounding the growth chamber and cells ensures that all the particles that are not pumped out just condense on the cold walls. The effusion cells are mounted so that the atomic beams condense directly on the sample holder, capable of continuous azimuthal rotation, and usually referred as CAR. Lastly the chamber is usually equipped with a reflection high energy diffraction (RHEED) set-up to monitor in real time some aspect of the growth (such as planar growth rates, or crystalline state of the substrate). The machine at NBI also has a separate buffer chamber, where degassing of the substrates takes place, to prevent any contamination of the growth chamber. In figure 1.2 a technical drawing illustrating the set-up of the MBE at NBI is shown.

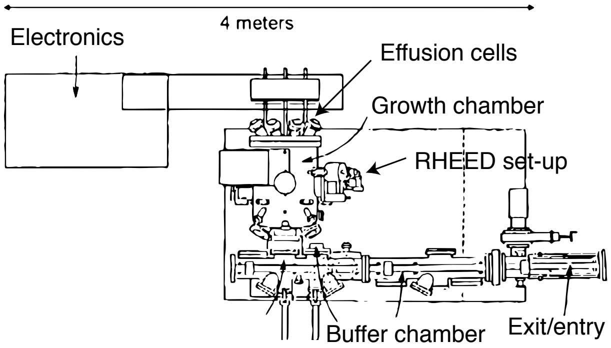

Figure 1.2: MBE technical drawing showing the basic element of a research grade machine.

The set-up at SPring8 synchrotron is inherently *dirtier* because of the technical difficulties of setting up a separate buffer chamber while having the instrument connected to a surface diffractometer. The general procedure to grow nanowires goes as follows: lithographically patterned substrates, fabricated following the procedures reported in chapter 2, are loaded and degassed at 250°C, then transfered to the growth chamber where, under a backpressure of As[1], they are annealed at 530° C to desorb the native oxide. The temperature of the substrate is then lowered to the desired growth temperature, and an accurate measurement of the temperature is given by an ir pyrometer facing and focused only on the sample's surface. The growth is then started by opening the shutter of the In source.

---

[1] It is well known that As desorbs from the surface at around 250° C, using an As backpressure keeps the substrate free from unwanted degradation of the surface

Technicalities aside MBE is best described with one sentence: "*spray painting …with atoms* "[34].

1.1.2 Nanowire growth

The first, and surely the most cited, encounter with nanowires dates back to the seventies; at that time nanowires were called nanowishkers [40]. The main features reported by Wagner and Ellis [40] were the evidence of the vapor-solid-liquid (VLS) growth mechanism and the possibility of single crystal growth without the introduction of defects during growth. Fast forward to today and the VLS mechanism is still indicated as the chief culprit of nanowire growth, although the growth models have been polished and expanded, the basic concepts are still the same and are described in the next paragraphs. The VLS mechanism, as the name implies, considers three main thermodynamic phases[2]: a liquid phase, a solid phase, and a vapor phase. Let's now consider a semiconductor substrate with a certain melting point. If we deposit another material with a lower melting point (either in the form of defined islands or a film thin enough that upon heating coalesces into island) there exist a certain temperature window where the substrate maintains its solid phase but alloys with with the deposited material. If the temperature is higher than the melting point of the deposited material a liquid alloy is formed, and to minimize its energy it will take a shape close to a droplet depending on the surface energy of the substrate. If we now introduce a vapor, in the form of atomic fluxes or a flow of gas, the liquid droplet is the preferred site for atom deposition from the vapor. The liquid droplets act as sinks and they become supersaturated. The absorbed material then diffuses through the liquid alloy to the liquid/solid interface (the growth interface) and precipitates a solid phase thus starting the growth. The liquid to solid transition at the growth interface is driven by a free energy minimization process and the growth rate at the growth interface is enhanced with respect to the rest of the substrates giving rise to freestanding nanowires. In thermodynamic language this reads as follows. We can write the fundamental equation of thermodynamics for the free Gibbs energy of a closed system:

$$dG = -SdT + VdP + \sum_{i}^{n} \mu_i dN_i \tag{1.1}$$

where n is the number of the species in the system and N_i is the number of the i-th specie. By considering an isobaric and isothermal process, which is the case for the VLS model of crystal growth, the chemical potential μ is defined as:

$$\mu_i = \left(\frac{\partial G}{\partial N_i}\right)_{T,P,N_{j\neq i}} \tag{1.2}$$

and the condition to have nanowire growth is:

$$\delta\mu_{vapor} > \delta\mu_{liquid} > \delta\mu_{solid} \tag{1.3}$$

where the zero of the chemical potentials is chosen to be the equilibrium value. A schematic representation of the VLS process is reported in figure 1.3.

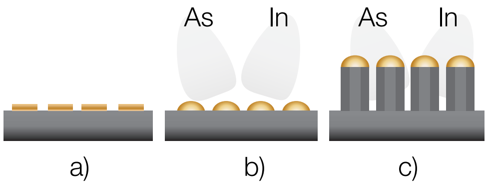

Figure 1.3: The VLS mechanism. a) The patterned substrate is heated to the alloying temperature. b) The substrate and the catalyst particles form a liquid alloy, the atomic beams are switched on. c) The growth of freestanding nanowire begins.

The driving force of the growth process is essentially described in equation 1.3 where the first inequality determines the supersaturation of the catalyst droplets. In general for MBE growth the driving force is strong, meaning that the system is driven far away from equilibrium. In such a regime we can not expect to model the system only using classical thermodynamics, because the kinetics of the process may be too slow for equilibrium to settle. Although nanowire growth has been historically described with equilibrium thermodynamics, in the past decades it has been realized that it

---

[2] A thermodynamic phase is a region in space throughout which most of the physical (i.e. temperature, pressure, composition, state of matter) properties have the same value.

must be instead described taking in account its highly non-equilibrium nature. In section 1.5 a general formalism to describe nanowire growth kinetics is introduced. The growth process is in general material dependent and since in this thesis the material system considered is only InAs further details are valid only for this systems.

1.2 Crystal Structure

A perfect crystal is a solid-sate-material whose constituents are arranged in a periodic fashion in all dimension. As such a crystal can be virtually broken down into one single repeating unit, the *unit cell*; then, a crystalline lattice can be constructed by stacking the unit cell in three dimension filling all the available space. If an operation like this can only be done in smaller domain of the material then it's no longer a crystal but rather a poly-crystal. The boundaries between each domain, or grain, are called grain boundaries.

Let's now consider an infinite arrangement of points. If it can be described by a set of translations in space, from an arbitrary origin, described by an equation in the form of 1.4:

$$\mathbf{R} = n_1\mathbf{a_1} + n_2\mathbf{a_2} + n_3\mathbf{a_3} \tag{1.4}$$

where $\mathbf{a_1}, \mathbf{a_2}, \mathbf{a_3}$ are linearly independent vectors then the set of points forms a Bravais lattice, and the three vectors are called the *primitive vectors* of that lattice. It turns out that there exists only fourteen unique lattices, considering symmetry operations. Again each of these lattices can be visualized by its unit cell (for the avid reader a very nice graphical representation can be found in Hammond [21] page 85). A Bravais lattice is just a mathematical concept, but if we place an atom or a set of atoms in each lattice point, the *basis*, then that lattice describes a perfect crystal. In the real world crystal structures have often local defects in the stacking but let's forget that for now and see how we can navigate in the most unambiguous way a crystal lattice.

Let's now introduce the notation for describing directions and planes in a crystal. A shorthand notation which, to best of my knowledge is the only one in widespread use, is called the Miller indices notation. A specific plane is denoted with $(h\,k\,l)$, a set of symmetry-equivalent planes is denoted with $\{h\,k\,l\}$, a specific direction by $[h\,k\,l]$, and the equivalent set of directions by $\langle h\,k\,l\rangle$. It is implicit that the Miller indices reflect the symmetry of the unit cell chosen. In general one refers to the most common unit cell which may or may not be the primitive cell, i.e. the unit cell with the smallest volumes. It is usual, and actually more practical to work with unit cells that show the lattice's symmetry. It is useful to introduce also the concept of *zone* which is a set of planes whose intersections are parallel and *zone axis* which is the common direction the plane in a zone share. To determine crystal directions symbols the following steps are taken: fist, select a direction of interest, making sure that it passes through the origin (usually selected as the back left-hand corner point of the unit cell, labeled as **000** in figure 1.4), then pick any point along the direction and take the coordinates as fractions of the **a**, **b**, **c** vectors, lastly express the coordinates whole numbers. For example, point **G** in figure 1.4, has coordinates 0,$\frac{1}{2}$,1 so the Miller symbol of the orange direction the points belong to is $[0\,1\,2]$; it is easy to see that any point on the direction will do for the calculation of the Miller symbol.

To describe planes the same procedure as described in the previous paragraph is used, but the intersections of the plane with the three base vectors are used to determine the symbol of the plane, as shown in figure 1.4b. The cubic system is chosen as it's the easiest example to work out, but the procedure is the same for any system.

Zinc blende (ZB) and wurtzite (WZ) are the most common crystal structures in the realm of binary semiconductors, especially for III-V compounds [44]; table 1.1 lists the experimentally stable crystal structure for selected compounds in bulk.

	N	As	Sb
Al	WZ	ZB	ZB
Ga	WZ	ZB	ZB
In	WZ	ZB	ZB

Table 1.1: Experimentally stable crystal structure of selected compounds, table adapted from [44].

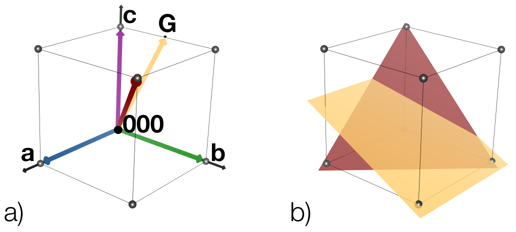

Figure 1.4: a) Miller symbols for directions in a cubic crystal; the Miller symbols for the red, green, blue, purple directions are $[1\,1\,1]$, $[0\,1\,0]$, $[1\,0\,0]$, $[0\,0\,1]$. Collectively purple, blue and green direction are symmetry equivalent so they are usually denoted as $\langle 1\,0\,0\rangle$. b) Miller symbols for planes in a cubic crystal; the Miller symbols for the red and orange plane are $(1\,1\,1)$, $(0\,1\,2)$. The reader may have noticed that orthogonal directions and planes share the same hkl values. This is peculiar for the cubic crystal system and does not hold true for other systems.

The *zinc blende* structure belongs to the cubic system and can be visualized as two face centered cubic (fcc) lattices overlapped and shifted about their origin by $(\frac{1}{4},\frac{1}{4},\frac{1}{4})$ where each of the resulting sublattice is constituted by either group III or group V elements. Such a crystal structure has a striking similarity with the diamond structure, but it has reduced symmetry operations arising form the two element basis that forms the lattice. In particular the lack of a center of inversion makes the ZB structure polar in the $\langle 1\,1\,1\rangle$ directions, meaning that there exist two symmetry unrelated bulk surfaces that are either terminated either by a group V or III element, as such they are usually denoted with different notations: $\langle 1\,1\,1\rangle$B and $\langle 1\,1\,1\rangle$A, respectively. The ZB structure of InAs is reported as an example in figure 1.5.[3]

Peeking into the ZB structure (*in fact, any fcc structure*), from the $[1\,0\,\bar{1}]$ direction reveals that the close-packed stacking of atomic planes follows a **ABC** stacking pattern, meaning that layer A, B and C do not sit on top of each other; the atomic planes are composed of pairs of III-V atoms, and usually labeled monolayers (ML). An illustration of the ZB structure viewed along the $[1\,0\,\bar{1}]$, with $[1\,1\,1]$ facing up to highlight the stacking, is shown in figure 1.7a.

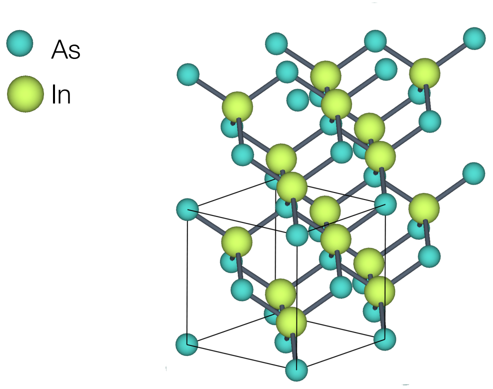

Figure 1.5: ZB crystal structure; the solid lines contour the unit cell.

The *wurtzite* structure belongs to the hexagonal system and consists of two hexagonal close packed (hcp) lattices shifted about their origin by (0,0,$\frac{3}{8}$) an example for InAs is reported in figure 1.6.

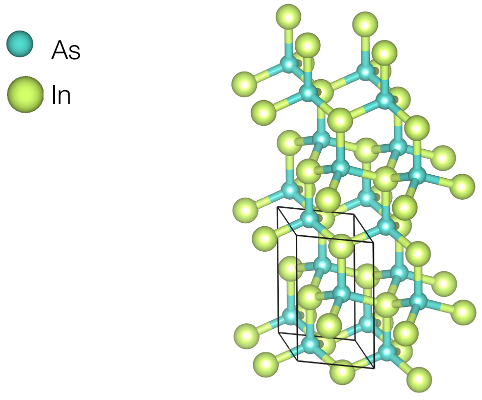

Figure 1.6: WZ crystal structure; the solid lines contour the unit cell.

It is convenient and in widespread use to use four indices $[hkil]$ to describe any hexagonal crystal. The

---

[3] All crystal structure drawings, unless noted are made with the software VESTA [35].

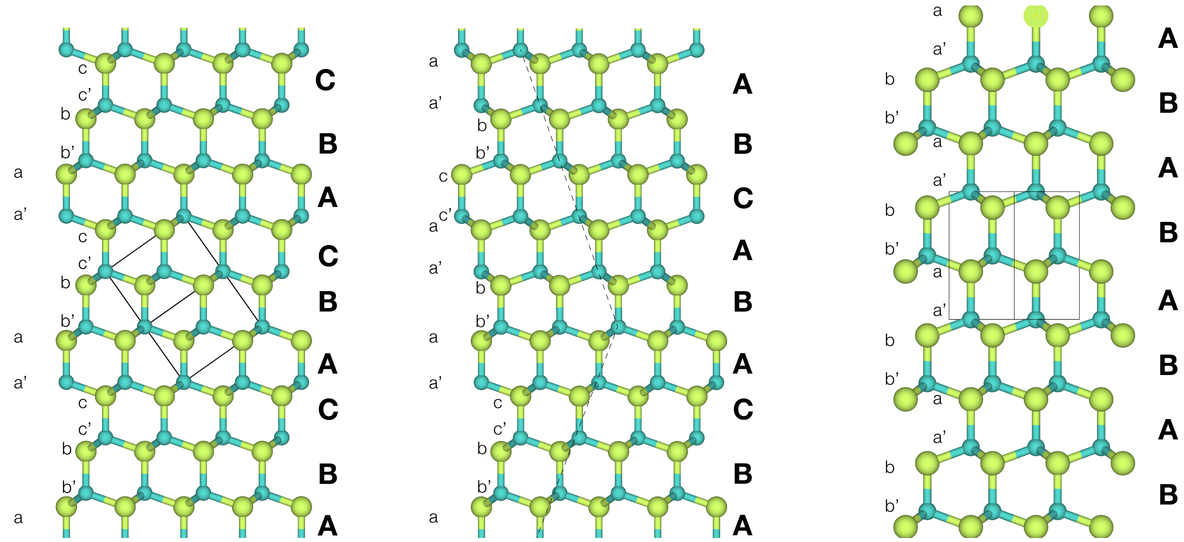

(a) View along the $[1\,0\,\bar{1}]$ direction, with $[1\,1\,1]$ facing upwards for the ZB structure.

(b) View along the $[1\,0\,\bar{1}]$ direction, with $[1\,1\,1]$ facing upwards for the TW structure. The dashed lines are a guide to the eye to locate the twin boundary.

(c) View along the $[1\,1\,0]$ direction, with $[0\,0\,1]$ facing upwards for the WZ structure.

Figure 1.7: Crystal structures stacking; capital letters indicate monolayers, whereas lower case letters indicate the atomic planes of the monolayers. The unit cells are contoured with black lines.

two notation are linked by the following relation for i: $i = -(h + k)$. Using the four indices notation, the same criterion to determine if directions are equivalent can be applied both to hexagonal and cubic systems; namely, *directions having the same indices regardless of order or sign are equivalent*. It is worth noting, at the cost of confusing the reader, that it is common practice in the literature to index the WZ planes and directions using the ZB indices as reference, the rationale behind this indexing madness will be clear later in the text (but it's easy to grasp if one thinks about the fact the arrangement of atoms in the planes perpendicular to the growth direction is the same for WZ and ZB). For instance the facets of nanowires are labeled $\{1\,1\,2\}$ using the ZB Miller indices, and $\{0\,1\,1\,0\}$ using the WZ Miller indices. The directions pointing towards the vertices between facets is $\langle 1\,1\,0\rangle$ using the ZB indices and $\langle 1\,0\,0\,0\rangle$ using the WZ Miller indices.

Before before proceeding to the next section let's introduce the phenomenon of *twinning*; that is when different parts of a crystal are mis-oriented with respect to each other according to some symmetry rule (e.g. a rotation about one axis). In III-V semiconductors twinned ZB is often observed. Recalling the ZB stacking along $\langle 1\,1\,1\rangle$, **ABCABC**, we can induce twinning by introducing one extra layer in the sequence making it **ABC[AB|A]CBA**. The vertical line denotes where the extra layer is added and it's called twin boundary. Such a defect is usually denoted as rotational twin because the crystal structures below and above the twin boundary are related by a rotation, in this case about the $[1\,1\,1]$ axis by 60 degrees; a grahpical representation of the structure of twinned ZB is reported in figure 1.7b. In this thesis the twinned ZB structure is labeled TW.

In this section a description of the nanowires' crystal structure has been given; though far from being the most comprehensive, for which a whole book may be needed, it offers a primer to understand the rest of this thesis.

1.3 Reciprocal Lattice

The reciprocal lattice plays a fundamental role in the study of periodic structures, for example in crystal diffraction and can be defined as follows. Consider a set of points **R** constituting a Bravais lattice and a plane wave, $e^{i\mathbf{k}\cdot\mathbf{r}}$. Such a plane wave will have the same periodicity only for specific set of **k** it will have it. The complete set of wave vectors that yield plane waves with the same periodicity of the Bravais lattice is its reciprocal lattice. Analytically, if:

$$e^{i\mathbf{k}\cdot(\mathbf{r}+\mathbf{R})} = e^{i\mathbf{K}\cdot\mathbf{r}} \tag{1.5}$$

holds true for any **R** and **r** then we can write:

$$e^{i\mathbf{K}\cdot\mathbf{r}} = 1 \tag{1.6}$$

which defines the set of reciprocal vectors **K**. It is clear from the definition above that any reciprocal lattice is defined with reference to a Bravais lattice, as such it is usual to call them reciprocal and direct lattice spanning the direct and reciprocal space respectively. A trivial recipe for constructing the primitive vector of a Bravais lattice spanned by $\mathbf{a}, \mathbf{b}, \mathbf{c}$ is given in equation 1.7. It is easy to see that the reciprocal lattice of a Bravais lattice is itself a Bravais lattice.

$$\begin{aligned} \mathbf{b_1} &= 2\pi\frac{\mathbf{a_2}\times\mathbf{a_3}}{\mathbf{a_1}\cdot(\mathbf{a_2}\times\mathbf{a_3})} \\ \mathbf{b_2} &= 2\pi\frac{\mathbf{a_3}\times\mathbf{a_1}}{\mathbf{a_2}\cdot(\mathbf{a_3}\times\mathbf{a_1})} \\ \mathbf{b_3} &= 2\pi\frac{\mathbf{a_1}\times\mathbf{a_2}}{\mathbf{a_3}\cdot(\mathbf{a_1}\times\mathbf{a_2})} \end{aligned} \tag{1.7}$$

Moreover one can also see that families of planes in crystals are correlated to reciprocal vectors, namely, for any family of lattice planes separated by a distance *d* there exist reciprocal lattice vectors perpendicular to the planes, the shortest having length of $2\pi/d$ [3].

It is now easy to see that the Miller indices of a plane are the coefficients of the shortest reciprocal lattice vector normal to the plane, i.e. $\mathbf{o} = h\mathbf{b_1} + k\mathbf{b_2} + l\mathbf{b_3}$ where **o** is such a reciprocal vector. The Miller indices of crystal planes can thus be defined also in this way.

1.3.1 A note about Crystallographic indices

In this thesis two slightly different notations are used to index the reciprocal space. Namely, the *usual* Miller-index notation and the surface-index notation (also known as the low energy electron diffraction (LEED) convention). Up to this point only the usual Miller-index notation has been used. The surface-index notation comes in handy when dealing with $(1\,1\,1)$ surfaces. As mentioned before the in plane arrangement of atoms in this family of surfaces is hexagonal and thus it is convenient to use a coordinate system with the same symmetry. Given the basis of the cubic lattice: $\mathbf{a_1} = a_0\hat{\mathbf{x}}, \mathbf{a_2} = a_0\hat{\mathbf{y}}, \mathbf{a_3} = a_0\hat{\mathbf{z}}$, one of the possible basis that exhibits hexagonal symmetry is [17]:

$$\begin{aligned} \mathbf{a}_{\mathbf{1}}^{\mathbf{s}} &= \frac{1}{2}(\mathbf{a_1} - \mathbf{a_3}) = \frac{1}{2}a_0(\hat{\mathbf{x}} - \hat{\mathbf{z}}) \\ \mathbf{a}_{\mathbf{1}}^{\mathbf{s}} &= \frac{1}{2}(-\mathbf{a_1} - \mathbf{a_2}) = \frac{1}{2}a_0(\hat{-\mathbf{x}} - \hat{\mathbf{y}}) \\ \mathbf{a}_{\mathbf{3}}^{\mathbf{s}} &= \frac{1}{2}(\mathbf{a_1} + \mathbf{a_2} + \mathbf{a_3}) = a_0(\hat{\mathbf{x}} + \hat{\mathbf{y}} + \hat{\mathbf{z}}) \end{aligned} \tag{1.8}$$

where $\mathbf{a}_{\mathbf{3}}^{\mathbf{s}}$ is connecting the $(1\,1\,1)$ monolayers. The use of such a coordinate system makes it easier to index $(1\,1\,1)$ surfaces and the directions normal to them and will be ever more evident in the next sections.
In this thesis the use of the surface-coordinates system indices is denoted by a lowercase *s* superscript on the indices, i.e. $[1\,1\,1]^s$. The use of the cubic coordinate system is be denoted by a lowercase *c* superscript on the indices, i.e. $[1\,1\,1]^c$, whereas the hexagonal coordinate system with a lowercase *h* superscript on the indices, i.e. $[1\,1\,1]^h$. The four index notation is evident enough and so it is used without any superscript. The angle between the $\mathbf{a}_{\mathbf{1}}^{\mathbf{s}}$ and $\mathbf{a}_{\mathbf{2}}^{\mathbf{s}}$ is then 120, and using equation 1.7, the reciprocal vectors can be calculated:

$$\begin{aligned} \mathbf{a}_{\mathbf{1}}^{\mathbf{s}} &= \frac{4\pi}{3a_0}(\hat{\mathbf{x}} + \hat{\mathbf{y}} - 2\hat{\mathbf{z}}) \\ \mathbf{a}_{\mathbf{1}}^{\mathbf{s}} &= \frac{4\pi}{3a_0}(\hat{-\mathbf{x}} + \hat{\mathbf{y}} - \hat{\mathbf{z}}) \\ \mathbf{a}_{\mathbf{3}}^{\mathbf{s}} &= \frac{2\pi}{3a_0}(\hat{\mathbf{x}} + \hat{\mathbf{y}} + \hat{\mathbf{z}}) \end{aligned} \tag{1.9}$$

In conclusion the surface coordinate system is a hexagonal system that can be used to describe cubic system (ZB); the key feature is that it can be easily used to directly compare the out of plane structure, along $\hat{\mathbf{z}}$ direction, with other hexagonal systems, as shown for example in figure 1.10.

1.4 X-Ray Diffraction

Diffraction from a crystal
Let's consider two individual scatterers, separated by a distance **d** and a incident plane wave along a certain direction $\hat{\boldsymbol{n}}$ with a wavelength λ and a wave vector $\mathbf{k} = 2\pi/\lambda\hat{\boldsymbol{n}}$, as shown in figure 1.8. Constructive interference takes place only if the difference in the traveled path is an integer multiple of the wavelength[4] and a plane wave is observed in the $\hat{\boldsymbol{n}}^{'}$ direction with a wavelength λ and a wave vector $\mathbf{k}^{'} = 2\pi/\lambda\hat{\boldsymbol{n}}^{'}$.

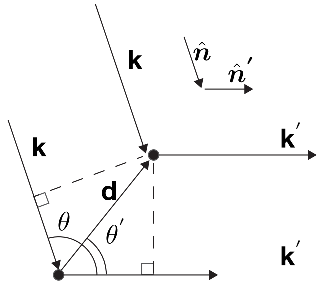

Figure 1.8: Illustration of the scattering geometry.

From figure 1.8 we can see that this condition translates to:

$$\boldsymbol{d}\cdot(\hat{\boldsymbol{n}}^{'} - \hat{\boldsymbol{n}}) = n\lambda \rightarrow \mathbf{d}(\boldsymbol{k}^{'}\cdot\boldsymbol{k}) = 2\pi n. \tag{1.10}$$

Adding complexity we can now consider an ensemble of scatterers conveniently placed in a Bravais lattice. Equation 1.10 then reads:

$$\mathbf{R}(\boldsymbol{k}^{'}\cdot\boldsymbol{k}) = 2\pi n \tag{1.11}$$

---

[4] It is subtly assumed that the scattering is perfectly elastic, i.e. the scattered photon does not lose any energy in the scattering event. This is largely true for all the experiments in this thesis but it must be noted that inelastic scattering can happen, especially near the absorption edges of the material and can give valuable informations.

or equivalently:

$$e^{i(\boldsymbol{k}'-\boldsymbol{k})\cdot\mathbf{R}} = 1 \tag{1.12}$$

for integer n and any **R** vector of the Bravais lattice. We can now state the Laue condition, remembering the definition of reciprocal lattice given in equation 1.6: *constructive interference will occur if the change in wave vector is a vector of the reciprocal lattice*. An alternative but equivalent condition, the Bragg's law, follows in equation 1.13 and figure 1.9; proof of the equivalence of the two conditions can be found in any solid state physics text book. The convenience of the reciprocal lattice should now be clear: a reciprocal space vector associated with a certain diffraction peak is perpendicular to the family of direct lattice planes scattering the incoming wave.

$$n\lambda = 2dsin(\theta) \tag{1.13}$$

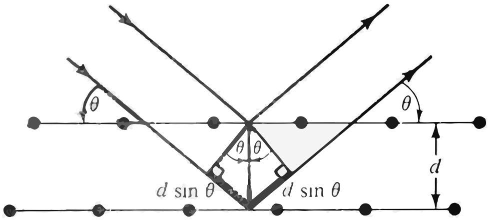

Figure 1.9: Example of a Bragg's reflection from a family of planes with spacing d; the path difference for the waves is $2dsin(\theta)$. Image adapted from [3].

Up to this point the nature of the incoming wave or of the scatterers is not considered, as such the obtained model is the most general possible. If we now consider X-rays with energies in the range 10-100 keV[5] we see that they are a good probe for inter-atomic distances in solids. To account for the nature of the scatterers, in this case electrons, we have to plug-in into the model their `ability' to scatter radiation. The elastic scattering of X-rays by a free electron is called Thomson scattering, and it is measured by the Thomson scattering length, or classical radius of the electron, r_0. The latter quantity can be derived classically or from a complete quantum mechanical treatment of the problem, neither is relevant for the aim of this thesis and both can be found in any solid state physics book. In the far-field limit, and neglecting multiple scattering events (the kinematic approximation) we can write the amplitude of the scattered waves from one atom as the integration of the electron density ($\rho(\mathbf{r})$) over the coherently illuminated volume:

$$A(\mathbf{K}) \propto \int \rho(\mathbf{r}) e^{i(\mathbf{K}\cdot\mathbf{R})} dr. \tag{1.14}$$

We can see that the scattered amplitude is thus proportional to the Fourier transformation of electron density of the atom, and it's referred to as the atomic form factor.

The structure factor The net amplitude of the scattered waves can be expressed as:

$$A(\mathbf{K}) \propto \sum_{j=1}^{n} f_j(\mathbf{K}) e^{i(\mathbf{K}\cdot\mathbf{d}_j)} \tag{1.15}$$

where $\mathbf{K} = \boldsymbol{k}' - \boldsymbol{k}$, $\mathbf{d}_j$ is the position vector of the j-th atom in the basis and n is the total number of the atoms and $f_j(\mathbf{K})$ is the atomic form factor of the j-th atom and includes all the required proportionality constants[6]. The atomic form factor is included in the structure factor because the structure factor not only depends on the position of the atoms but also on the nature of the atoms. One should also keep in mind that the symmetries of the unit cell can lead to a null structure factor. As such the intensity of the resulting Break is also zero and the reflection is called forbidden.

To get the full expression for scattered amplitude by

---

[5] These limits are chosen for two practical reason, the upper energy is low enough that we can forget about relativistic effects, whereas the lower bound ensure that experimentally the X-ray beam has an high penetration power in light materials such as beryllium, which is the material used in all the `windows' for X-ray instrumentations.

[6] Most atomic form factors have been calculated and are usually found as parametric functions in several crystallographic databases.

a crystal, we combine all the factors and writel:

$$A(\mathbf{K}) \propto \sum_{n} e^{i(\mathbf{K}\cdot\mathbf{R}_n)} \sum_{j} (\int \rho(\mathbf{r}) e^{i(\mathbf{K}\cdot\mathbf{R})} dr) e^{i(\mathbf{K}\cdot\mathbf{r}_j)}$$

$$= \underbrace{\sum_{n} e^{i(\mathbf{K}\cdot\mathbf{R}_n)}}_{lattice\ sum} \underbrace{\sum_{j} f(\mathbf{K}) e^{i(\mathbf{K}\cdot\mathbf{r}_j)}}_{structure\ factor\ F(\mathbf{K})} \tag{1.16}$$

where $\mathbf{R_n}$ is a lattice vector, $\mathbf{r_j}$ is the position of the atom in the basis.

Large structures in real space correspond to fine details in reciprocal space. On the other hand small structures in real space, like an electron or an atom correspond to intensity distributions in reciprocal space on a much broader scale. Thus the structure factor spans over several reciprocal lattice points and determines their intensity. Atomic form factors determine intensity distribution on even broader scale. The lattice sum, although conceptually very close to the other sum introduced, is in practice quite extraordinary; if one considers the amount of unit cells in a crystal it's easy to see that the sum of all the phase vectors is very close to unity except when the scattered waves are all in phase. In the latter case the lattice sum is equal to the sum of all the terms i.e. the numbers of unit cells and so it is a extraordinarily big number enhancing the scattering intensity and thus making Bragg's peaks sharp.

In conclusion the structure factor determines the intensity of a given Bragg reflection whereas the lattice sum determines the possible positions in reciprocal space.

Crystal truncation rods

A real crystal breaks one of assumption made in the previous sections, namely the lattice being infinite in all directions. If we consider a crystal with an infinite span in every dimension the scattered amplitude is a Fourier transform of the function describing its structure. Breaking the infinite periodicity in one dimension, say along z, which corresponds to the creation of a flat two dimensional surface perpendicular to said direction, can be modeled by multiplying the crystal structure by a step function i.e. $\mathcal{C}_{\text{truncated}} = \mathcal{C} \times \mathcal{H}(z)$, where $\mathcal{H}(z)$ is the step function. Invoking the convolution theorem we see that the Fourier transform of such a truncated structure is equal to the convolution of the Fourier transform of the original function describing the infinite crystal with the Fourier transform of the step function (i.e. an amplitude decaying proportionally to $1/K_z$), as shown in equation 1.18.

$$A(\mathbf{K}) \propto \mathcal{F}(\mathcal{C}_{\text{truncated}}) \propto \mathcal{F}(\mathcal{C}) * \mathcal{F}(\mathcal{H}) \tag{1.17}$$

$$\propto \mathcal{F}(\mathcal{C}) * 1/K_z \tag{1.18}$$

The result is that scattering is no longer localized in the Bragg's peaks but also around them with an intensity proportional to $1/(K_z^2)$ and in a direction perpendicular to the newly created surface; the effect is called crystal truncation rod (CTR). The above concept can be expanded in more dimension and with complex truncations but the result is always that a diffuse scattering can be observed around a Bragg peak over a volume in reciprocal space inversely proportional to the size of the truncated crystal and with streaks parallel to the truncated surfaces' normal. Modeling the exact general expression for the intensity evolution depends on the chosen shape function (for a flat plane the aforementioned step function) that describes the truncation of the crystal and goes beyond the scope of this thesis. As an example a detector image of CTR stemming from an InAs nanowire viewed with the growth direction facing up, is reported in figure 1.11a along its real space interpretation. In addition a reciprocal space map of a slice along the $(1\,1\,2)^c$ plane is reported in figure 1.11c along with its real space interpretation.

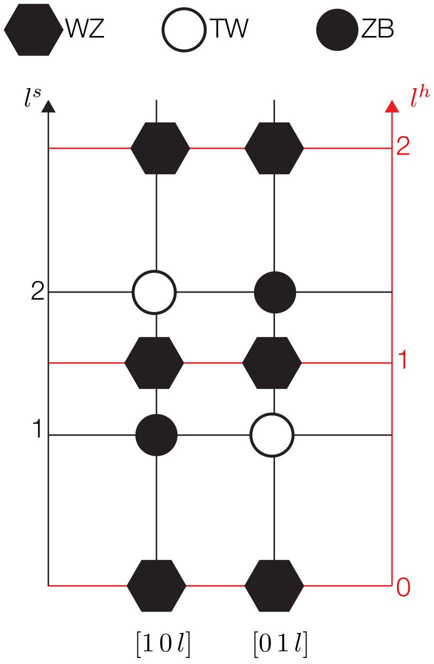

Figure 1.10: Location of Bragg peaks of WZ, and TW/ZB indexed using the surface coordinate system. ZB Bragg's peaks are expected for integer l_s but the structure factor makes some of these reflection forbidden (e.g. (1 0 2)). The fate of TW Bragg's peak is very close to that of ZB, except that the structure is rotated by 60 degrees and thus the Bragg's peaks are not forbidden where the ZB peaks are forbidden and vice versa. WZ has a smaller interplanar distance in real space and consequently the Bragg's peak are expected at multiples of 1.5 l_s.

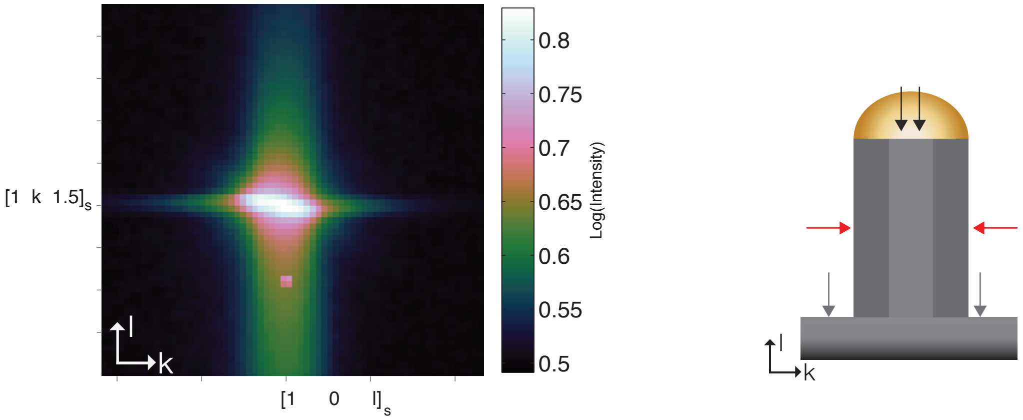

(a) Experimentally observed crystal truncation rod around the wurtizte peak of an InAs nanowire. The expected position of the Bragg peak of wurtizte is 1,0,1.5 in surface coordinates, and indeed a strong intensity is recorded; around this peak two distinct CTR are easily recognizable. The first streak extending in the *l* direction, i.e. the direction connecting two mono-layers in the $[1\,1\,1]$ cubic ZB direction, stems from both the limited height of the nanowire and the surface of the substrate. The second streak normal to the first and extending in the k direction, stems from the finite (in this case $\approx 100\text{nm}$) width of the nanowire.

(b) Real space model for the crystal structure that explains the crystal truncation rods reported in figure 1.11a. The red arrows highlight the finite width of the nanowires contributing with the streak along k. Whereas the black arrows denote the surface of the nanoiwre generating the truncation rod for l > 1.5, the gray arrow indicate the surface of the substrates generating the streak for l < 1.5.

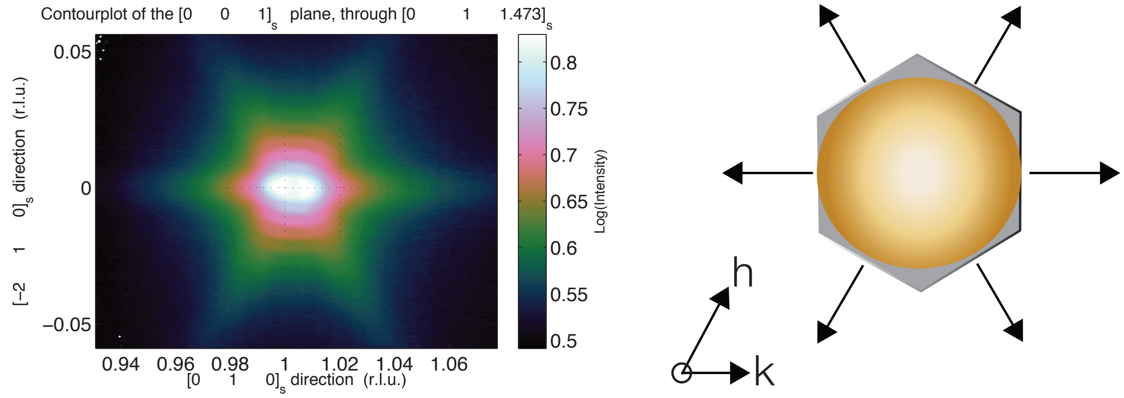

(c) Reciprocal space map around the WZ peak showing star-shaped truncation rods. The six streaks indicate the presence of six facets parallel the l direction in surface coordinates, consistent with the usual hexagonal morphology of the nanowires. Facets can be easily index as belonging to the $\{0\,1\,1\,\bar{0}\}$ family of planes.

(d) Top view of the real space model for the crystal structure that explains the crystal truncation rods reported in figure 1.11c. The reference surface coordinates are reported in the lower left corner, with l the growth direction point out of the paper plane. The black arrows highlight the family of $\{0\,1\,\bar{1}\,0\}$ facets.

Figure 1.11: Crystal truncation rod examples, 1.11a and 1.11c, show two different examples of measured truncation rods; figures 1.11b and 1.11d show the real space models to interpret the measured data.

1.5 General formalism for growth kinetics

Before introducing the theoretical formalism one should note that equilibrium thermodynamics is somewhat redundant phrasing: *thermodynamics* is by definition the study of equilibrium states, meaning that the state variables describing the system do not change in time. Whenever the a system is driven out of equilibrium thermodynamics are not strictly applicable but can be used as the limiting or reference scenario. The study of the rates at which out of equilibrium systems evolve is called *kinetics*. The most fascinating aspect of modern thermodynamics is the introduction of the concept of local equilibrium, explained in figure 1.12, which allows using all of the machinery of classical thermodynamics and interweave it with the non-local kinetics of the system. Using the same approach one can use continuum language to describe atomic transitions rates. In the next paragraph the theoretical formalism is introduced, following the approach by Krogstrup et al. [30], with the aim to introduce some of the concepts of nanowire growth that will later emerge from the X-ray experiments.

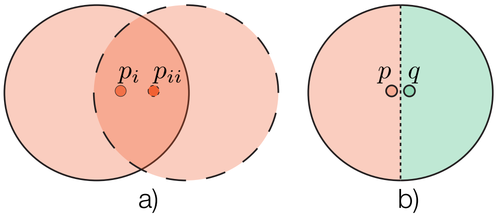

Figure 1.12: The Concept Of Local Equilibrium. a) For each thermodynamic state, such as the liquid sate, we can define a local state, p, described by the average properties of the surroundings (the local-ensemble) which is large enough to describe its constituents (i.e. p_i and p_{ii}), but also small enough to *survive*, i.e. maintain local equilibrium, when the whole system is driven out of equilibrium. b) The interface between two local states defines where two particles can be described only by the local ensemble they belong to (e.g. p and q).

Transition state theory

Atomistic models of nanowire growth, such as those based on density functional theory (DFT) [18] or on molecular dynamics models [42], exist and offer estimations for specific and relevant energies. On the other hand atomistic models often lack a direct link with the experimentally controllable parameters, such as temperature and especially the impinging atomic fluxes. The possibility of describing atomic transitions with a continuum language as proposed by Krogstrup et al. [30], is a way to bridge the gap between the complicated atomistic description and the overall growth dynamics, as a function of fluxes and temperatures, which can be experimentally measured, for instance with in-situ studies. The goal is to being able to predict a given growth experiment based on dynamical simulations. However, this is a big challenge due to the complicated mechanisms of nanowire growth, and a lot of improvement in both understanding and simulation techniques still needs to be done. In the following paragraph the formalism is introduced; the thermodynamic quantities are introduced in figure 1.13.

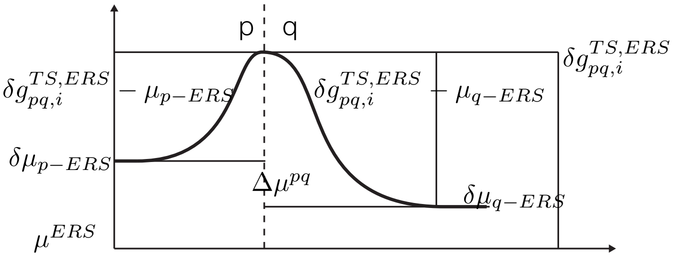

Figure 1.13: One dimensional illustration of the free energy barrier associated with a transition to state q from state p. We assume that the transition state barrier is symmetric $\delta g^{TS,ERS}_{pq,i} = \delta g^{TS,ERS}_{qp,i}$, which means that if a transition from state p to state q happens, the energy barrier to go from q to p remains unchanged.

The probability of a $p \to q$ transition follows an Arrhenius dependence, i.e. $P_{pq,i} \propto e^{-\frac{\delta g^{TS}_{pq,i}}{k_b T}}$ where the subscript pq, i means from state p to state q for the specie i, T is the temperature and k_b the Boltzmann constant; $\delta g^{TS}_{pq,i}$ is the activation energy of the transition state (TS) that is the difference in free energy per atom between the state p and the TS. The activation energy can also be written as $\delta g^{TS}_{pq,i} = \delta g^{TS,ERS}_{pq,i} - \delta\mu_{p-ERS,i}$ where the TS free energy and the chemical potential are now calculated with respect to a conveniently chosen equilibrium reference state (ERS), as described in figure 1.13.

We can now describe the mean flux of atoms crossing the pq boundary from state p per unit area with the following equation:

$$\Gamma_{pq,i} \begin{cases} \Xi_{pq,i}\bar{c}_{p,i} e^{-\frac{\delta g^{TS,ERS}_{pq,i} - \delta\mu_{p-ERS,i}}{k_b T}} & \text{(1.19a)} \\ \qquad \text{if } \delta g^{TS,ERS}_{pq,i} \geq \delta\mu_{p-ERS,i} & \\ \Xi_{pq,i}\bar{c}_{p,i} & \text{(1.19b)} \\ \qquad \text{if } \delta g^{TS,ERS}_{pq,i} \leq \delta\mu_{p-ERS,i} & \end{cases}$$

where $\Xi_{pq,i}$ is a prefactor accounting for the number of attempts per atom of species i to transition from state p to state TS per unit time and unit area and its form depends on the type of transition. $\bar{c}_{p,i}$ is the density of specie i atoms in the state p, which corresponds to the probability of the state being populated. Equation 1.19b describes a barrier-free transition. In general the form of both $\Xi_{pq,i}$, and $\bar{c}_{q,i}$ are unknowns and so we want to find a relation to other thermodynamic parameters. To do so we can for instance evaluate the total flux $\Delta\Gamma_{pq,i} = \Gamma_{pq,i} - \Gamma_{qp,i}$ across pq for a symmetric barrier, i.e. $\delta g^{TS,ERS}_{pq,i} = \delta g^{TS,ERS}_{qp,i}$. Moreover if we evaluate $\Delta\Gamma^{ERS}_{pq,i}$ with the ERS superscript meaning that we evaluate the total flux across pq at equilibrium; then detailed balance must hold i.e. $\Delta\Gamma^{ERS}_{pq,i} = 0$. The pq and qp fluxes can be written as:

$$\Gamma^{ERS}_{pq,i} = \Xi_{pq,i}\bar{c}^{ERS}_{p,i} e^{\frac{\delta g^{TS,ERS}_{pq,i}}{k_b T}} \tag{1.20}$$

$$\Gamma^{ERS}_{qp,i} = \Xi_{qp,i}\bar{c}^{ERS}_{q,i} e^{\frac{\delta g^{TS,ERS}_{qp,i}}{k_b T}} \tag{1.21}$$

where the chemical potentials in the exponential have vanished because the equations are evaluated at equilibrium. We can then write:

$$\Delta\Gamma^{ERS}_{pq,i} = 0 \rightarrow \Xi_{qp,i} = \Xi_{pq,i}\frac{\bar{c}^{ERS}_{p,i}}{\bar{c}^{ERS}_{q,i}} e^{\frac{\delta g^{ERS}_{pq,i} - \delta g^{ERS}_{qp,i}}{k_b T}} \tag{1.22}$$

The total flux is:

$$\begin{aligned} \Delta\Gamma_{pq,i} = \Gamma_{pq,i} - \Gamma_{qp,i} = & \\ \Xi_{pq,i}\bar{c}_{p,i} e^{-\frac{\delta g^{TS,ERS}_{pq,i} - \delta\mu_{p-ERS,i}}{k_b T}} & \\ - \Xi_{qp,i}\bar{c}_{q,i} e^{-\frac{\delta g^{TS,ERS}_{qp,i} - \delta\mu_{q-ERS,i}}{k_b T}} & \end{aligned} \tag{1.23}$$

using equation 1.22 to replace Ξ_{qp} in equation 1.23, the total flux can be written as:

$$\begin{aligned} \Delta\Gamma_{pq,i} &= \Xi_{pq,i}\bar{c}_{p,i} e^{-\frac{\delta g^{TS,ERS}_{pq,i} - \delta\mu_{p-ERS,i}}{k_b T}} \\ &- \Xi_{pq,i}\frac{\bar{c}^{ERS}_{p,i}}{\bar{c}^{ERS}_{q,i}}\bar{c}_{q,i} e^{-\frac{\delta g^{ERS}_{pq,i} - \delta g^{ERS}_{qp,i}}{k_b T}} e^{-\frac{\delta g^{TS,ERS}_{qp,i} - \delta\mu_{q-ERS,i}}{k_b T}} \end{aligned} \tag{1.24}$$

factoring out common terms:

$$\begin{aligned} \Delta\Gamma_{pq,i} &= \Xi_{pq,i} e^{-\frac{\delta g^{TS,ERS}_{pq,i}}{k_b T}} \\ &\quad \times \left(\bar{c}_{p,i} e^{\frac{\delta\mu_{p-ERS,i}}{k_b T}} \right. \\ &\quad \left. - \frac{\bar{c}^{ERS}_{p,i}}{\bar{c}^{ERS}_{q,i}}\bar{c}_{q,i} e^{\frac{\delta g^{ERS}_{qp,i}}{k_b T}} e^{-\frac{\delta g^{TS,ERS}_{qp,i} - \delta\mu_{q-ERS,i}}{k_b T}} \right) \\ &= \Xi_{pq,i} e^{-\frac{\delta g^{TS,ERS}_{pq,i}}{k_b T}} \left(\bar{c}_{p,i} e^{\frac{\delta\mu_{p-ERS,i}}{k_b T}} - \frac{\bar{c}^{ERS}_{p,i}}{\bar{c}^{ERS}_{q,i}}\bar{c}_{q,i} e^{\frac{\delta\mu_{q-ERS,i}}{k_b T}} \right) \end{aligned} \tag{1.25}$$

A simpler case is a barrier free transition, like in 1.19b, where $\delta g^{TS,ERS}_{pq,i} \leq \delta\mu_{p-ERS,i}$ and the atomic flux can be written as:

$$\Delta\Gamma_{pq,i} = \Xi_{pq,i}\left(\bar{c}_{p,i} - \frac{\bar{c}^{ERS}_{p,i}}{\bar{c}^{ERS}_{q,i}}\bar{c}_{q,i} e^{-\frac{\delta g^{TS,ERS}_{pq,i} - \delta\mu_{q-ERS,i}}{k_b T}}\right) \tag{1.26}$$

Remembering the definition of Gibb's energy $g = h - Ts$ where h is the enthalpy, s is entropy and t is temperature [7]. Then $dg = dH - Tds - sdT \rightarrow dg =$

---

[7] we use lowercase letters to denote densities of the related extensive variables, i.e. g is the Gibb's energy per atom

$dh - Tds$ at constant temperature. We can then substitute into equation 1.25 to isolate the prefactors including the entropy term in one, which can then be used as a temperature independent fitting parameter. So we define:

$$\Xi_{pq,i}^{'} = \Xi_{pq,i} e^{\frac{ds_{pq,i}^{TS,ERS}}{k_b T}} \tag{1.27}$$

To describe the system we need to extend and refine the thermodynamic states introduced in the simple VLS picture earlier. In particular we add the adatom and beam flux sates, where the first one describes the atoms that are adsorbed but not incorporated on any surface, and the second one describes the atoms comprising the direct beam flux; moreover we redefine the vapor state as the state of the gas phase atoms not belonging to the primary beam i.e. mainly atoms evaporated or remitted from neighboring surfaces. In summary for MBE growth we can distinguish five main states for each element i: beam flux (b, i), vapor (v, i), solid (s, i), adatom (a, i) , liquid (l, i), as shown in figure 1.14.

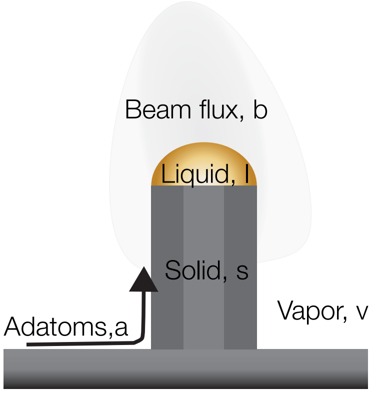

Figure 1.14: The five thermodynamical states considered in the growth model.

We distinguish different pathways for the incorporation of atoms in the liquid phase: al and $(vb)l$ that is adatom to liquid and gas (both vapor and beam flux state) to liquid; moreover we distinguish three more main transitions for the adatoms: aa, av, as that is diffusion, desorption, incorporation respectively; lastly, the ls transition that is liquid to solid transition which is responsible for the formation of the newborn crystal. In figure 1.15 the pathways are schematically drawn.

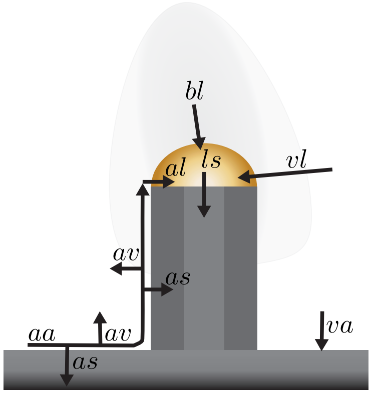

Figure 1.15: The main transitions paths in nanowire growth. aa, av, as are diffusion, desorption, incorporation respectively; ls is liquid to solid transition; al and $(vb)l$ are tthe adatom to liquid and gas (both vapor and beam flux state) to liquid respectively.

As shown in Krogstrup et al. [27] and Krogstrup et al. [30] we can describe the atomic flow through the liquid phase with a mass transfer equation, calling N_l the number of atoms in the liquid phase:

$$\frac{d}{dt} N_l = I_{III} + I_V - I_{inc}. \tag{1.28}$$

where I_i are the sorbption currents in the liquid, for elements of the i specie and I_{inc} is the incorporation current from the liquid to the solid. I_i can be written as:

$$I_i = \int \Delta\Gamma_{al,i} dl_{TL} + \int \Delta\Gamma_{(vb)l,i} dA_{vl} \tag{1.29}$$

where the first term describes the adatom to liquid current, and the second term the gas to liquid current. The two integrals are evaluated over the total length of the vapor-liquid-solid triple line (TL), and the area of the liquid droplet respectively; the integration limits are not specified in the second integral because they can be approximated differently, see for example Glas [19]. A

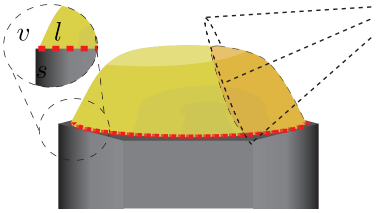

Figure 1.16: Description of the triple line and liquid-vapor collection area. The TL line is represented as the red dashed line, running along the droplet edges. As shown in the upper left inset the TL is in contact with liquid, vapor and solid phase. The liquid vapor collection area, shaded in a dark yellow,consist only on the area that is actively intercepting the atomic beam, represented as the dashed *cone*.

graphical description of the TL and the area is given in figure 1.16.

Using equation 1.19 we can write for a lv transition:

$$\Gamma_{lv,i} = \Xi_{lv,i} e^{\frac{-dg_{lv,i}^{ERS}}{k_b T}} \bar{x}_{l,i} e^{\frac{\delta\mu_{l-ERS,i}}{k_b T}} \tag{1.30}$$

and for a vl transition:

$$\Gamma_{vl,i} = \Xi_{vl,i} e^{\frac{-dg_{vl,i}^{ERS}}{k_b T}} \bar{x}_{v,i} e^{\frac{\delta\mu_{l-ERS,i}}{k_b T}} \tag{1.31}$$

where $\bar{x}_l$ is the atomic fraction in the liquid phase for specie i; evaluating 1.31 at the ERS:

$$\Gamma_{vl,i}^{ERS} = \frac{P_i^{ERS}}{\sqrt{2\pi m k_b T}} = \Gamma_{lv,i}^{ERS} = \Xi_{lv,i} \bar{x}_{l,i}^{ERS} e^{-\frac{dg_{lv}^{ERS}}{k_b T}} \tag{1.32}$$

where we have used the detailed balance and set the chemical potential to zero because we are at the ERS; the second equality is simply due to mass conservation[8]. We can then rewrite 1.30, using 1.32:

$$\Gamma_{lv,i} = \frac{P_i^{ERS}}{\sqrt{2\pi m k_b T}} \frac{\bar{x}_{l,i}}{\bar{x}_{l,i}^{ERS}} e^{\frac{\delta\mu_{l-ERS,i}}{k_b T}} \tag{1.33}$$

Equation 1.33, is the same as writing:

$$\Gamma_{lv}(x_i, T) = \frac{P(x_i, T)}{\sqrt{2\pi m k_b T}} \tag{1.34}$$

where $P(x_i, T)$ is the equivalent vapor pressure of an infinite large liquid phase with a composition x_i, at temperature T . We can then write:

$$P_(x_i, T) = P^{ERS} \frac{\bar{x}_{l,i}}{\bar{x}_{l,i}^{ERS}} e^{\frac{\delta\mu_{l-ERS,i}}{k_b T}} \tag{1.35}$$

$P_(x_i, T)$ and $\delta\mu_{l-ERS,i}$ can be measured independently and are in good agreement[9]. If we consider a barrier free sorption and single vapor species we can write:

$$\Delta\Gamma_{(vb)l,i} \approx f_{b,i,\perp} + f_{v,i,\perp} - \Gamma_{lv,i} \tag{1.36}$$

where $f_{b,i,\perp} + f_{v,i,\perp}$ is the total impinging flux (from the beam and from the vapor) and we don't have a lb transition as it's non physical.

We can now write down the liquid sorption currents:

$$I_{(vb)l,i} = \int \Delta\Gamma_{(vb)l,i} dA_{vl} = f_{b,i,\perp} + f_{v,i,\perp} - \Gamma_{lv,i}$$
$$\approx A_{vl} \left(f_{v,i,\perp} - \frac{P_i^{ERS}}{\sqrt{2\pi m k_b T}} \frac{\bar{x}_{l,i}}{\bar{x}_{l,i}^{ERS}} e^{\frac{\delta\mu_{l-ERS,i}}{k_b T}} \right) + A_{vl}^{'} f_{b,i,\perp} \tag{1.37}$$

where we have used equation 1.33 and we consider the projected area $A_{vl}^{'}$ only for the bv transition, whereas we use the full area of the droplet since the v phase is surrounding the whole droplet;

$$I_{al,i} = \int \Delta\Gamma_{al,i} dl_{TL}$$
$$\approx l_{TL} \Xi_{al,i}^{'} e^{-\frac{\delta h_{al,i}^{TS,ERS}}{k_b T}} \left(\bar{c}_{a,i} e^{\frac{\delta\mu_{a-ERS,i}}{k_b T}} - \frac{\bar{c}_{a,i}^{ERS}}{\bar{c}_{l,i}^{ERS}} \bar{c}_{l,i} e^{\frac{\delta\mu_{l-ERS,i}}{k_b T}} \right) \tag{1.38}$$

Moreover we can write the flux for the va transition using the same reasoning used to obtain equation 1.33:

$$\Gamma_{va,i} \approx f_{b,i,\perp} + f_{v,i,\perp} - \frac{P_i^{ERS}}{\sqrt{2\pi m k_b T}} \frac{\bar{\rho}_{a,i}}{\bar{\rho}_{a,i}^{ERS}} e^{\frac{\delta\mu_{a-ERS,i}}{k_b T}} \tag{1.39}$$

---

[8] one can see that by realizing that at equilibrium what goes *out* of the liquid can not be more that what goes into the liquid from the vapor phase

[9] Private conversation with Peter Krogstrup, no reference possible

where ρ_i is the density of adatoms of the i specie.

Explaining the formalism to model the aa, as and av transitions in detail goes beyond the scope of this thesis but a qualitative description follows to get intuitive feeling. Diffusion or aa happens when adatoms move around a surface until a energy favorable transition can happen, modeling the surface diffusion requires to specify the rate at which the transition happens and the energy dependence of the motion with respect to the crystal structure. Also diffusion is in general driven by a gradient of a thermodynamical potential (such as chemical potential, temperature, pressure) and this has also to be taken into account for modeling. Diffusion is ended either by as or av transition that is incorporation on the crystal structure or desorption. One of the key difference between the two transitions (referred in general as *death* events, whereas a $vb-a$ transition is called *birth* event) is that desorption can take place anywhere whereas incorporation requires an available site as required by the fixed 1:1 stoichiometry of the solid. Desorption is in general easier to model as it's a thermally activated transition, meaning that the adatom needs to reach a certain energy before the transition can happen, which means that an equation in the form 1.19 can be used. The distance *traveled* between a birth and death event is denoted diffusion length and referred to as λ it is convenient to define the collection areas as λ_s for the substrate and λ_w for the nanowires side facets. Only adatoms on the NW sidewalls with a distance of less than the effective diffusion length, λ_w, to the growth interface can effectively contribute to the growth. Adatoms on the surface need first to travel on the substrate and then reach the growth interface.

Let's now focus on the ls transition; for VLS growth we distinguish between two different families of transitions usually referred to as nucleation free growth and nucleation limited growth. In the first situation the ls transition is limited by the transfer of single III-V pairs to the growth front. In the second situation the ls transition is limited by the formation of a small nucleus i.e. there exists another energy barrier greater than the single pair transition state barrier. Moreover we also consider two different regimes: TL is in contact with the top facet (regime I) or the TL is no longer in contact with the top facet (regime II). It is however rather uncertain exactly when and under which growth conditions the growth proceeds with a regime I or regime II [30]. In general the amount of group V species in the liquid phase is low compared to the group III, keeping that in mind and using equation 1.25 we can write the rate for a single pair ls transition as:

$$\begin{aligned}\Delta\Gamma^{X}_{ls,III-V} &= \Xi_{ls,III-V}\, e^{-\frac{\delta g^{TS,ERS}_{ls,III-V}}{k_b T}} \\ &\times \left(x_v e^{\frac{\delta\mu_{l-ERS,III-V}}{k_b T}} - x_v^{ERS} e^{\frac{\delta\mu^{X}_{s-ERS,III-V}}{k_b T}} \right)\end{aligned} \tag{1.40}$$

Although the chemical potentials with respect to the ERS are not introduced, we use the superscrpit X to highlight the fact that the chemical potential of the solid phase depended on the location of the nucleation event, and the system morphology. To perform a complete modeling one needs to specify a complete set of X parameters. Moreover the chemical potential of the liquid $\delta\mu_{l-ERS,III-V}$ must be an oscillating function because of the nucleation limited growth, i.e. it must decrease right after a nucleation event and then rise again to reach a critical level to nucleate.

For the VLS mechanism the catalyst particle has to be liquid, but the state of the particle has been under a lot of investigations since the seventies. At the usual growth temperature for Au-catalyzed InAs nanowires one should expect a solid particle, based on the binary phase diagrams for Au and In (eutectic temperature of 455 °C) and considering that the solubility of As in Au is close to being undetectable (i.e. around 1% at.). Yet experimental evidence suggest that the catalyst particle is liquid during growth [7, 22, 29, 37]. Although some report [12] that the catalyst particle remains solid during growth, one should not forget that nanowire growth is a far from equilibrium process and thus phase diagrams can be misleading as they are valid only at equilibrium. Moreover the system is a ternary system rather than binary and the presence of As, even if in extremely low concentration can play a significant role. Lastly the Gibbs Thomson effect could also play a role; the equation quantifying the change in chemical potential of a given compound, with the morphology of a droplet, as function of its size is:

$$\mu = \frac{4\gamma v_c}{d} \tag{1.41}$$

where v_c is the atomic volume, γ is the surface energy and d is the diameter. Considering the temperature dependence of the chemical potential we can write:

$$T_m - T = \frac{4\sigma v_c}{d\Delta S_m} \tag{1.42}$$

where T_m is the melting point, and ΔS_m is the entropy of melting; in principle with equation 1.42 one could estimate the magnitude of the melting point depression due to size effects, however finding the values for σ and ΔS_m is not trivial because they are dependent on the composition of the droplet and the structure of the interface [38]. A brutal but instructive approximation is to use the values for pure gold [25] which yields a melting point depression of just 1 % which does not explain the experimental evidence. Tchernycheva et al. [37] proposes that the thermal history of the sample is relevant as a strong hysteretic behavior is observed. Indeed after the annealing step (T≈ 540 °C) the catalyst is surely a liquid alloy, and the fast temperature ramp to reach the growth temperature can lead to the phenomena of supercooling i.e. there exists a nucleation barrier which prevents the liquid to freeze into a solid state even though the temperature is below the eutectic temperature. For the remainder of this thesis the gold catalyst is thus considered liquid during growth.

In this section a primer on the complex topic of growth dynamics has been given. It goes without saying that the introduction given is far from being complete, as the dynamical modeling requires to solve numerically a number of coupled equations (some of which have been shown above) and find or estimate the relevant thermodynamic parameters. Nonetheless several important quantities have been described and will be later used to explain the result from the in-situ X-ray measurements.

2 | Substrates For Nanowires Growth

Substrates for nanowire growth are, as already mentioned in section 1.1.2, composed of a semiconductor with a clean surface and a catalyst of some sort deposited on top. In this thesis we consider only lithographically defined gold particles as the catalyst but in general different alternatives are available. A very detailed review article covering the alternatives to gold assisted nanowire growth was recently published by Dick and Caroff [10]. In this chapter I will explain the general process to fabricate substrates, the role of substrates in nanowire growth and lastly report the progress I obtained in the fabrication process.

2.1 Substrate preparation with electron beam lithography

Electron beam lithography is a pattern transferring technique in which a focused electron beam is scanned on top of a surface covered with a material sensible to electrons exposure, either by lowering (negative resist) or by increasing (positive resist) its solubility in a given solvent. The result of the exposure to a focused beam is that the chains of the positive (negative) resist are broken (cross-linked) when hit by electrons. The substrates developed in this thesis are based on InAs $(1\,1\,1)$ surface with positioned arrays of gold droplets. Arrays are defined with electron beam lithography and can have arbitrary shapes, different lattices and well defined orientations. A brief summary of the fabrication process follows in the next paragraphs and detailed description is attached in appendix .1. I have mostly used epi-ready[1] semiconductor substrates without any further cleaning before processing. Semiconductor substrates are extracted from their vacuum packaging slips only in clean environments (either a class 100 clean room, or a class 10.000). The substrates are then prepared for electron beam lithography by coating them with polymeric resist, cf. figure 2.1a. The desired pattern is exposed either with a electron beam lithography system running at 20 kV (Raith eLiNE 100) or 100 kV (Elionix ELS-7000) and chemically developed, cf. figure 2.1b and c. After the lithography step substrates are plasma-ashed to remove any leftover trace of resist in the developed pattern, chemically etched or ion-milled to remove oxide on the surface of the exposed areas and loaded in a e-gun evaporator where the desired amount of gold is deposited, cf. figure 2.1d. The deposited metal is then removed via chemical lift-off, leaving just the desired amount in the exposed regions cf. figure 2.1e. Finally, to achieve the cleanliness required to avoid any contamination of the MBE growth

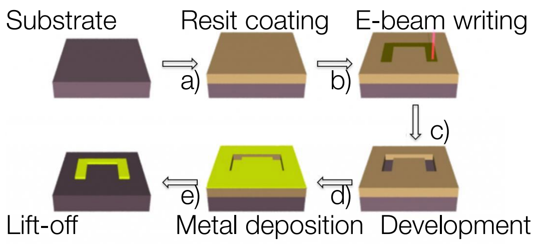

Figure 2.1: Electron beam lithography process. Refer to the text for the description of the steps. Image adapted from [1].

---

[1] Epi-ready stands for ready for epitaxial growth and denotes a semiconductor substrate that has been capped with a high quality oxide to preserve the surface from aging. In practice epi-ready substrates are the *cleanest* off-the-shelf substrates available.

chamber, substrates are plasma ashed and dipped in HF right before being loaded in the exit entry chamber of our system. The specific steps used to fabricate substrates for nanowire growth are reported in figure 2.2.

2.2 Challenges

Although most of the steps required are very common in the nanofabrication world they can be more challenging for substrate fabrication for the following reasons. The size of the substrate, up to two inches, can introduce strongly nonuniform resist thickness. Moreover the sheer number of exposed features can pose technical challenges also for the most modern e-beam systems, for instance a very common substrate, an array with a square lattice of dots with a 5μ pitch covering one quarter of a two inch substrate, can contain 25×10^6 features. Lastly the need for high precision on small features (a very common size for a feature is around 50 nm) over tens of millimeter scale areas requires an extremely stable software and hardware. Judging from the sky-high number and variety of software and hardware crashes experienced during my thesis I forecast that some more years are required before hardware and software reach the point where a lot of substrates can be made without a considerable amount of sleepless nights. Another important note about lithography is the choice of the write-field size, which determines how much the beam can move before the stage is moved. As a rule of thumb the smaller the write-field the better the exposure because the beam doesn't get de-focused/stigmated by the deflection coils, but at the same time the exposure times can get longer; I have found a good compromise at 300 μm for 100 kV and $600\mu m$ for 30kV. The ashing step is the most crucial as it can drastically reduce the yield of nanowires if the ashing time is too short or if omitted completely, whereas the subsequent cleaning step can be safely omitted because the thin oxide present will diffuse and desorb at growth temperature without being *trapped* at the gold/semiconductor interface as experimentally observed during this thesis, and foreseeable considering the phase diagram of the oxide most likely to from that is indium oxide [36].

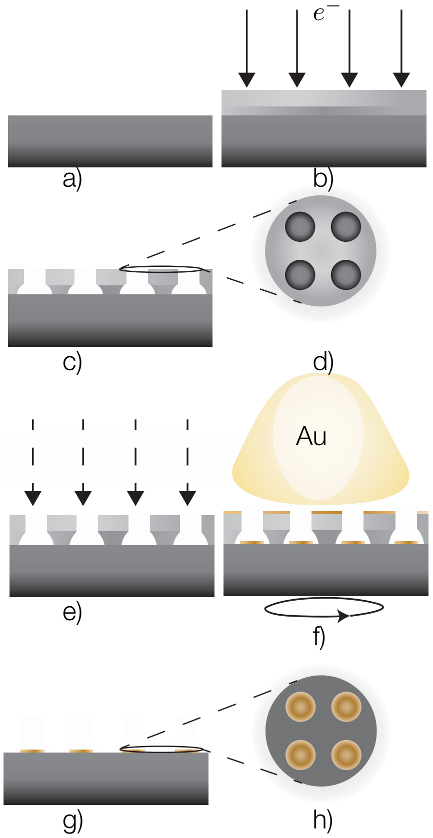

Figure 2.2: Schematic description of the main steps involved in the fabrication of a substrate for nanowire growth. a) The bare InAs substrate. b) Double layer resit is spun on and the chip is lithographically patterned. c) After development the exposed features are now ready to be used as a mask, the use of a double layer resit with the bottommost layer being more sensible to exposure creates an undercut making the lift-off process easier. d) Top view of the substrate after development, e) Substrate is cleaned with plasma ashing to remove traces of resit from the exposed features. f) Au is deposited with an electron gun with a constant rotation of the substrate to obtain an uniform thickness. g) The unexposed resit and the unwanted gold film are removed with the lift-off. h) Top view of the finished substrate.

2.3 Results

The substrates' characteristics determine the position and to a certain extent the size of the nanowires. The control of the individual positions of nanowires is of paramount importance not only for future's device integration but also to craft substrates that allow fundamental studies on nanowire growth dynamics, as reported for instance by Madsen et al. [31]. Such a control can be obtained by placing the catalyst's particles in arrays with well-defined pitches and shapes (for example in figure 2.3 a SEM micrography showing a $85\mu m \times 85\mu m$ square array is shown) or even single lines with e-beam lithography.

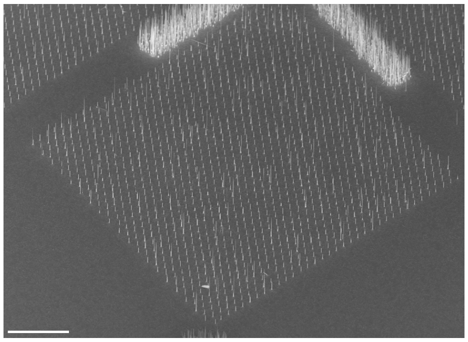

Figure 2.3: SEM micrography of a $85\mu m \times 85\mu m$ square array, in the upper right conner an alignment mark (i.e. a cross) is visible, hinting at the possibility of making arrays of nanowires with shapes only limited by the creativity of the researcher. Scale bar is $20\mu m$.

A representative micrograph of a square array of catalyst droplet is shown in figure 2.4.

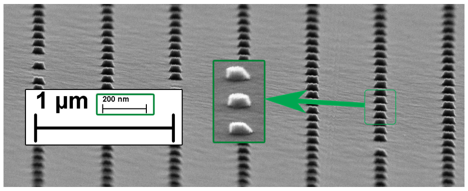

Figure 2.4: SEM micrography of Catalyst array, image taken at 70 degree angle of tilting.

The volume of the catalyst particle controls to some extent the size of the nanowires although the size of the nanowire is also strongly dependent on the growth conditions. For the same growth conditions the diameter of the nanowires scales with the volume of the droplets; to this time and to the best of my knowledge no fundamental relation has been found yet. During growth the effective size of the catalyst particle is determined by the $\frac{V}{III}$ ratio and in turns determines different growth modes and the resulting crystal structure of the nanowires as reported by Krogstrup et al. [28] and discussed in 3.3.1. The crystal orientation and chemical composition of the substrates influence the adatoms' motions on the surface, as mentioned in section 1.5; for instance diffusion on a GaAs $(1\,1\,3)$ surface is significantly different from InAs $(1\,1\,1)$ at the same temperature.

Size control of the gold droplets is obtained by carefully tuning the e-beam exposure parameters. The diameter of the exposed holes in the resist, figure 2.2d), depends on the dose (i.e. the number of electrons going through the resist) which can loosely defined as:

$$number \quad of \quad electrons \propto T_{dwell} \times I_{beam} \tag{2.1}$$

where T_{dwell} is the amount of time the electron beam stays still in a position on the specimen, and I_{beam} is the beam current. To measure the size of the catalyst droplets automated SEM imaging is employed, where the SEM is programmed to take images in specific regions of interest; the inherent flatness of the sample and an auto-focus algorithm ensure that the microscope is always in focus. In this way it is possible to obtain an high number of images, almost covering the whole sample without manual interaction. Each image taken is around 3 megapixels, and for every region of interest at least hundreds of images are take, ensuring high precision in every image and good statistics due to the big number of independent measurements. Every image is then fed to a software able to extract the relevant informations. The description of the software I developed is reported in appendix .3, along with the a link to its source code.

In figure 2.5 the measured radius as function of dose for different pitches is shown; the reported measures were performed on square array exposed at 30 kV.

Hexagonal arrays and single lines with the same pitch were also measured an the results were inside the error bar of the reported measurements.

It's clear from figure 2.5 that the size of the particle can be tuned over a wide range. Although a minor nuisance comes from the *proximity effect*, a general phenomenon in e-beam lithography: two exposure with the exact same parameters can produce features with different sizes depending on their local surroundings. For example a square array of dots, with a pitch of 5 μm will have bigger diameters than a square array of dots with a pitch of 10 μm for the same dose.

This can be easily seen in figure 2.5 and it's further highlighted in figure 2.6. Although the proximity effect can be corrected with sophisticated softwares, the most robust solution is still to make extensive dose testing to quantify the magnitude of the effect and correct manually the dose when producing the final substrates. It is well known that the proximity effect is strongly dependent on the acceleration voltage of the electron beam, decreasing with increasing voltage [4]. In figure 2.7 the same investigation on the proximity effect is reported for a 100 kV electron beam, confirming indeed that the proximity effect is negligible being below the detection limits of the measurement technique. Lastly in figure 2.8 the measured radius as function of dose is reported for an electron beam at 100kV, showing the same tunability as for the lower acceleration voltage but with an increased precision. It is worth spending some words on the precision of both the fabrication process and measurements. In all the figures the errorbars are the statistical error on the measurements and do not take into account the resolution of the SEM itself $\approx$ 2 nm; due to the high number of measurements the error on some measurements it is below the precision of the SEM and so it has little physical meaning and it's just a measure of how *good* the image analysis procedure really is. It is very clear from all the reported measurements that a 100 kV electron beam gives a much higher precision, as also suggested by the MonteCarlo simulation reported in appendix .2. Moreover exposure at 100 kV are faster, as much as three times, making the result less sensible to machine instabilities such as stage drifting over time, unstable beam currents.

In conclusion not only the amount of deposited gold but also the diameter of the catalyst droplet can be finely tuned giving a great freedom to control the size of the nanowires.

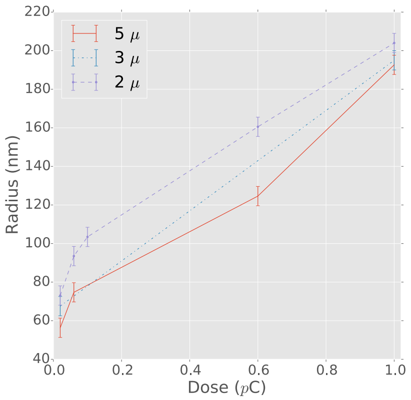

Figure 2.5: Catalyst size, for square arrays with three different pitches (2,3,5 μm), as function of dose at 30 kV, 5 nA beam current, 20 μm aperture.

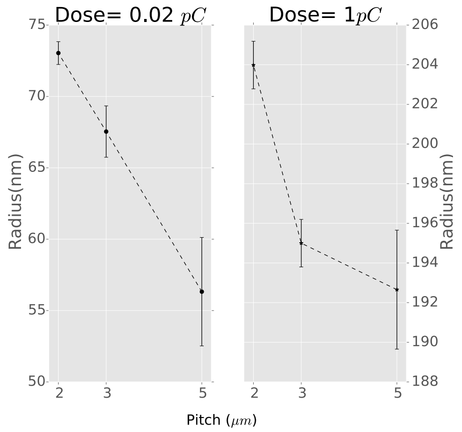

Figure 2.6: Proximity effect for a low dose exposure (left pane) and high dose exposure (right pane). The proximity effect becomes less relevant as the feature size increases. Error bars on the measurements are the error of the mean of the $n > 1000$ measurements.

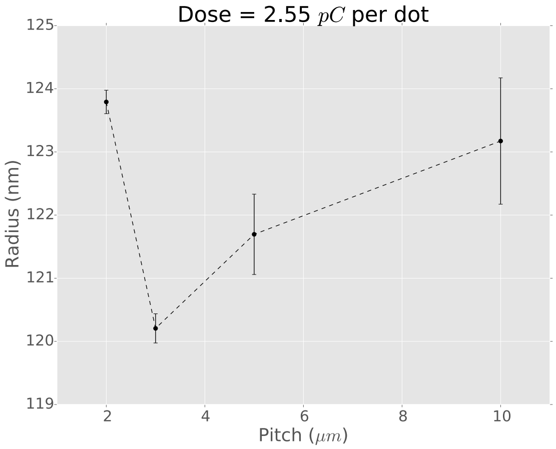

Figure 2.7: Proximity effect at 100kV. In this case the proximity is undetectable. The error bars on the measurements are the error of the mean of the $n > 1000$ measurements. It is possible to conclude that an high acceleration voltage produces more uniform arrays.

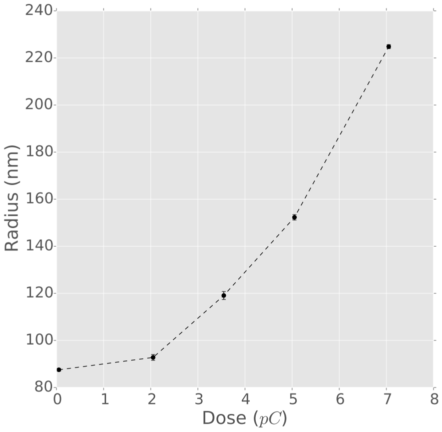

Figure 2.8: Catalyst size for a square array with $10\mu m$ pitch as function of dose at 100 kV. Exposure is done with 10 nA beam current using a 120 μm aperture.

2.3.1 Substrates for Nanowire Networks

Size and position control are the requirements to make nanowires truly useful for any application. The next step is however combining size and position control to create increasingly complex architectures based on one dimensional components. A variety of novel structures has been reported, from branched and *hyper*branched structures [41] to nanotrees [11]. One of the most promising architecture is a position controlled nanowire network, as reported for instance by Dick et al. [13]. Nanowire networks are indicated as on of the most promising system to perform braiding of Majorana's fermions [2, 39]. Moreover the possibility of creating networks of nanowire based transistor could in principle open new ways for the endless quest of miniaturization of electronics [43]. Additionally, branched structures, such as T, X shapes and nanotrees, offer exquisite engineering freedom for fundamental physics studies in multi-terminal devices.

In this section we will focus on the fabrication of substrates for nanowire networks. There exist different approaches to create nanowires networks the most promising being sequentially seeded nanowires [13] or controlled kinking and branching by growth parameter engineering. We use the latter technique to growth InAs networks. We either use a Ga pulse [26] or a quick drop in the growth temperature to promote kinking; the kinking process is shown in figure 2.9. Although the process is not simple and the growth parameters need to be tuned promising structures have been observed during the period of this thesis.

To obtain a nanowire network is essential to understand and control the morphology and crystal structure of the nanowire. We know that our InAs nanowires grow in the $[0\,0\,0\,1]$ direction (parallel to the $[1\,1\,1]_c$ of the substrate) and have hexagonal morphology with $\{0\,1\,\bar{1}\,0\}$ facets, cf. section 1.11d. Moreover we know that they have WZ crystal structures and the kinked branches are found to be growing in the $\langle 1\,1\,2\rangle_c$ directions with a trapezoidal morphology.

To make sure that nanowires meet, thus forming a network, hexagonal arrays of gold droplets are aligned

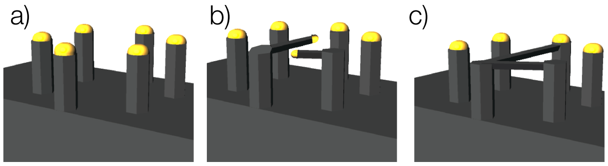

Figure 2.9: Nanowire kinking process. a) A short stem is grown. b) Either a short gallium pulse or a quick temperature drop make the kinked growth start. The catalyst droplet is now at the end of the branch. c). Branches grow along the $\langle 1\,1\,2\rangle_c$ direction eventually meeting the stems of other nanowires.

with respect to the $[1\,\bar{1}\,0]$ direction of the ZB substrates. The catalyst particles then *sit* along the $\langle 1\,1\,2\rangle_c$ directions of the substrate, as shown in figure 2.12. The $[1\,\bar{1}\,0]$ direction is chosen because it's the major flat of the commercial wafers (cf. figure 2.10 and figure 2.12) and also the related $(1\,\bar{1}\,0)$ planes are the cleavage planes, being the lowest order non-polar planes, which makes the direction always easy to determine with optical or electron microscopy.

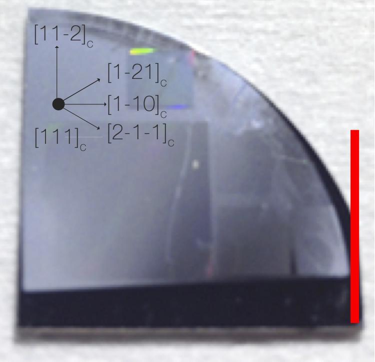

Figure 2.10: Picture of a substrate after growth. The red line highlights the major flat of the wafter which is by convention the $[1\,\bar{1}\,0]$ direction of the crystal. The slightly more opaque and iridescent areas on the substrate are the arrays of nanowires.

It is also possible to make the droplets in the hexagonal arrays bigger and smaller alternatively, thus altering the radial and axial growth rate of the nanowires (cf. figure 2.11, top panel). With this technique one could

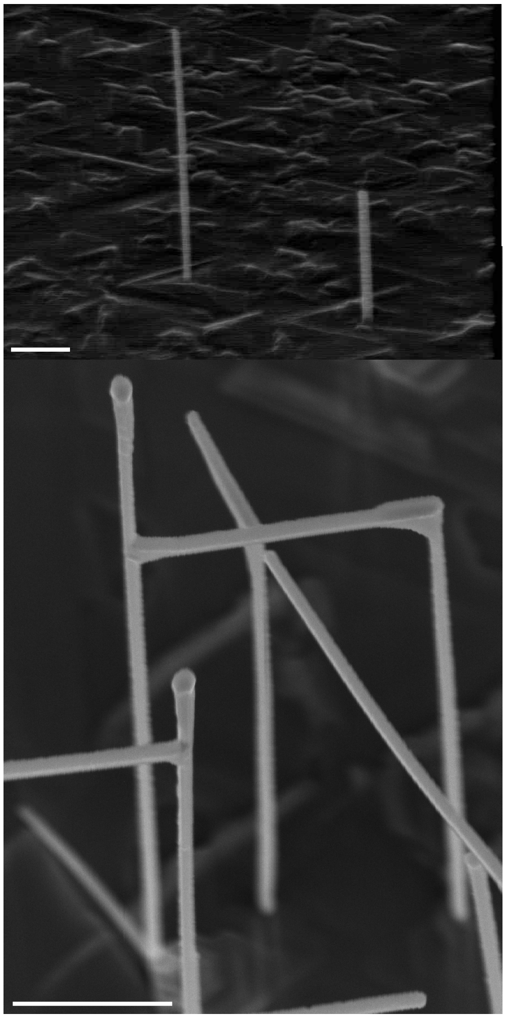

Figure 2.11: Top panel, SEM micrograph of two adjacent nanowires grown with particles of different diameter. Bottom panel two nanowires (grown on catalyst with different diameters like in the top panel) are connected forming an h shaped structure. Scale bars are 10 μm in both panels.

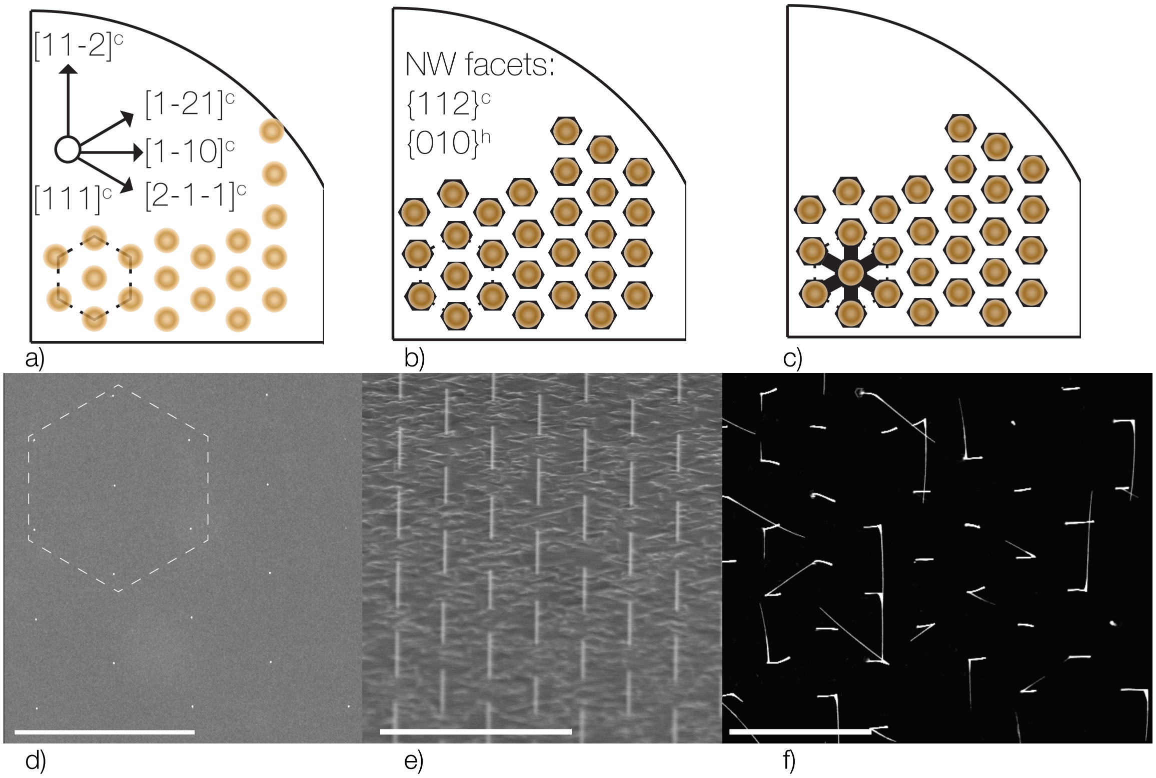

Figure 2.12: Step by step process to obtain NWs networks. Top row, schematic top view drawing of the process, the $[1\,1\,1]$ direction of the substrates is pointing out of the paper. The outer shape of the drawing mimics the real shape of the substrate as reported in figure 2.10. Bottom row SEM micro-graphs of the same steps, images are taken at an angle to highlight the orientation of the nanowires; the scale bar are in all the micrographs is $10\mu m$. b) and e) Nanowires are grown in the $[1\,1\,1]_c$ direction. c) and f) The nanowires grown in the step before act now as stems for the branches to grow, we can only see growth along the than $\{1\,1\,0\,0\}$ (or $\{1\,1\,2\}_c$.

implement extremely complex architectures, because the kinking event and the growth of the branch happens at different heights, or may not happen at all for a given combination of growth conditions and droplet size. As a proof of concept of this technique in figure 2.11 bottom panel, is reported a simpler connected structure shaped like a lower case *h*. Going from the simple proof of concept to a fully controllable network still requires further investigations.

2.3.2 Novel substrates whit SiO$_2$

I also experimented with a novel class of substrates, namely InAs $(1\,1\,1)$ surfaces with a thin film SiO_2 deposited on top, on which holes are patterned and etched away and *filled* with gold to act as a catalyst for growth. The aim is to be able to growt nanowires while minimizing the parasitic epitaxial growth in-between the wires. Such a system could be in fact of great importance when studying in-situ growth dynamics with X-ray because it should allow to completely separate the signal from the nanowires and from the substrate. This is discussed in details in chapter 3. Here only the fabrication process is explained. The fabrication procedure is almost the same as for the *standard* substrates described in the previous section, except that a thin film of SiO$_2$ is evaporated with a deposition system before the lithography step. Then, right before the gold deposition step, holes in the SiOp_2 film are etched away using ion milling. In appendix .1 the calibration of the ion milling Kaufman source is reported. In figure 2.13 the fabrication steps are described, whereas in figure 2.14 a cross section SEM micrograph shows the final morphology of the holes and deposited gold *droplet*. Before the beam-time this family of substrate was tested with the in-house MBE at NBI, where it was found that with similar growth condition as the standard substrates nanowire growth is possible. We also noticed that the growth is extremely sensible to the HF dip before loading. Growing with the same condition but with a substrate which had seen a shorter HF dip did not result in any nanowires. No further analysis of this effect is performed but this show how sensible the growth conditions are with respect to surface diffusion, the only thing which likely can be changed by the length of the HF dipping step. To the best of my knowledge growth on such substrates has never been reported before and although our investigation need further analysis the obtained results are promising. The effect of a thicker film (we have used 20 nm) different cleaning procedures, or the use of wet etching instead of ion milling could be further explored in the future.

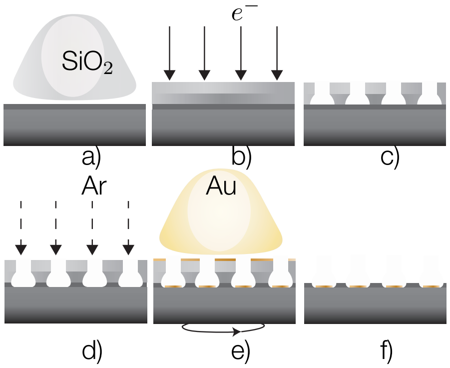

Figure 2.13: Schematic description of the main steps involved in the fabrication of the SiO$_2$ family of substrates. a) the bare InAs substrate with a thin film of SiO$_2$ deposited. b)Double layer resit is spun on and the chip is lithographically patterned. c) After development the exposed feature are now ready to be used as a mask. d)Holes in the SiO$_2$ thin film are created with Ar ion milling. e) Without breaking the vacuum Au is deposited with an electron gun under rotation of the substrate. f) The unexposed resit and the unwanted gold film are removed with the lift-off.

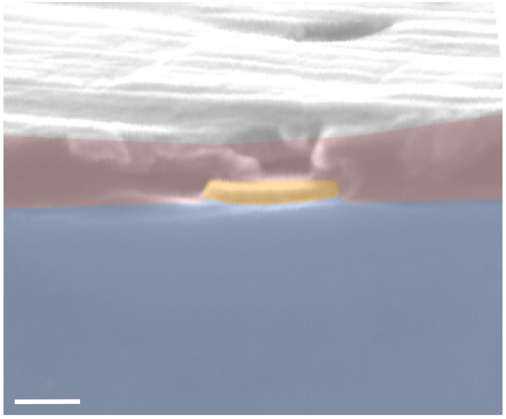

Figure 2.14: Representative cross section SEM micrograph of Sio$_2$-InAs substrates. The false colors help to highlight the different layers: in blue the bulk InAs substrate, in red the thin film of Sio$_2$, and in yellow the deposited gold. The scale bar is 100 nm.

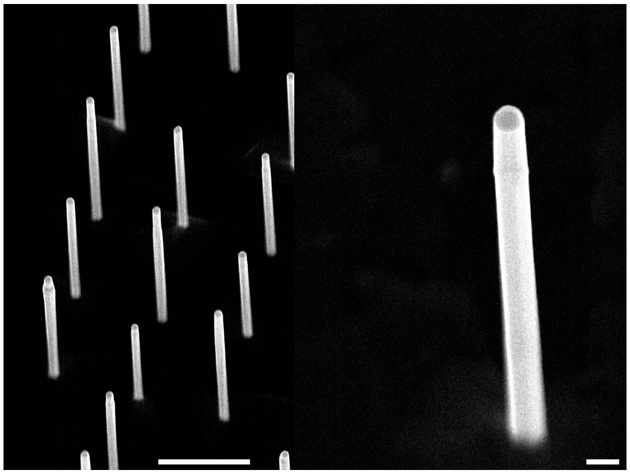

Figure 2.15: InAs nanowires on SiO_2 and InAs substrate, fabricated using the procedure outlined in 2.13; left panel shows an overview of the array, the length and diameters of the nanowires are uniform, suggesting that the holes and the gold droplets they contain are uniform across the array.The scale bar $1\mu m$. In the right panel single wire close-up showing the usual faceting of the nanowire. Scale bar is 100 nm.

3 | In Situ X-ray Diffraction from InAs Nanowires

The purpose of these experiments (performed in two different beam-times) is to analyze the growth dynamics and the mechanisms controlling the crystal structure formation during Au-catalyzed InAs nanowire growth by MBE. To the best of my knowledge, no in-situ study on Au-catalyzed InAs nanowire growth has been reported so far. By studying the dynamics of the growth is it possible to understand many details such as the structural and morphological evolution of both the nanowires and the substrates. The growth mechanisms of nanowires still raise many fundamental questions and this is also due to the experimental challenges associated with characterization of nanowires while they grow. Although in-situ TEM studies [22], [7], [45] can give valuable information often the nanowires are grown with extremely low beam fluxes because of the limitations of the UHV requirements of TEM.
X-ray scattering alone can not answer all the questions, so post-growth TEM and STEM measurements are performed in collaboration with Sriram Venkatesan at Max-Planck-Institut Düsseldorf.

Two types of measurements are performed, namely time resolved measurements and reciprocal space maps. The basics of these kinds of measurements are explained in the following paragraphs.

Time resolved measurements

Time dependent measurements are carried out at a constant sample position during the nanowire growth and are intended to study the growth kinetics and structural evolution. The sampling time is set by the detector integration time and the readout time. The first is chosen to maximize the signal to noise ratio the latter depends on a combination of the actual firmware capabilities of the detector and the capabilities of the software and hardware at the beamline. During the first beamtime (reported in section 3.3) the time resolution was limited at 0.5 seconds due to firmware limitations, whereas during the second beam time (reported in section 3.2) the limitations were completely bypassed by talking directly to the detector and the time resolution was 0.2 seconds.
To analyze the huge amount of data I developed an application able to quickly parse and display the detector's images. A technical description and a link to the source code is reported in appendix .3.

Reciprocal space maps

Reciprocal space mapping (RSM) is performed during the steady state periods when the In shutter was closed and the growth halted. RSMs give an insight on morphology and amount of different structures in the sample by measuring the diffuse scattering around a Bragg's reflections. Whenever the growth is stopped one has the freedom to move the detector around; since it's possible to correlate each single pixel to a hkl set it is possible to map the reciprocal space[32, 33], hence the name of *Reciprocal space mapping*.

3.1 Experimental Set-up

The in-situ MBE growth chamber at the Spring8 synchrotron at the BL11XU beamline gives a unique possibility to perform characterization of the structural evolution during the nanowire growth. The MBE setup is mounted on a surface diffractometer equipped with an area detector Pilatus 100Ks. The diffractometer is the 4S+2D type, i.e. four axes for orienting the sample and two axes for positioning the detector. The MBE chamber is equipped with five Knudsen cells and the RHEED system. Be windows are welded onto the chamber and allow incoming and outgoing angles up to 45 degrees measured from the sample surface and in-plane scattering angle up to 120 degrees. Asymmetric Bragg reflections allow separate analysis of the different crystal structures present in the nanowires and the substrate, mainly WZ, ZB and TW and their respective CTRs.
The X-ray beam from the undulator source is monochromatized to photon energies of 20 keV with a beam size of 0.5 mm ^{2}. The sample is aligned by the beamline scientist in the beam with respect to the instrument coordinate system and put in the Bragg condition around the WZ peak at $[1\,0\,1\,.\,5]_s$, cf figure 1.10. The Ewald sphere going through the WZ peak comes close enough to the ZB and TW peaks, resulting in strong peaks from all three structures present simultaneously on the area detector. During growth no rotation of the substrate is possible in order to keep the Bragg condition; this may induce inhomogeneities in the growth of the nanowires across the sample. An overview of the experimental set up is reported in figure 3.7.

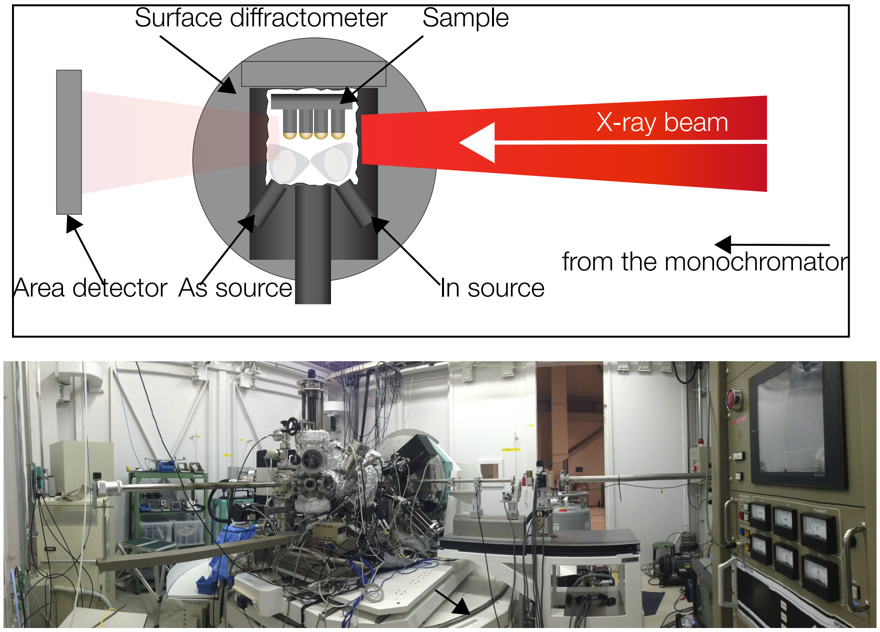

Figure 3.1: In-situ MBE at BL11XU beamline. Top panel schematic drawing with key components labeled. Bottom panel: photograph of the set-up inside the hutch.

3.2 Growth dynamics

InAs $(1\,1\,1)$ wafers are cleaved to 1cm^2 pieces and the substrate are prepared for nanowire growth as explained in section 2; the design, a square array with a 500 nm pitch completely covering the whole sample, guarantees that the X-ray signal is coming from the array of nanowires (the sample is aligned so that the X-ray beam hits at the center); the pitch is chosen so that the signal is intense enough but the array is not so dense that the growth conditions are altered because of intense shadowing effects (i.e. nanowires competing for growth material). The sample is then glued to a Molybdenum block specifically designed for the MBE setup at SPring8 with Indium glue to maximize thermal contact. The substrates are annealed at 530° C to desorb the native oxide under As back-pressure as explained in section 2. RHEED is used to monitor the state of the sample surface. As soon as the RHEED pattern transform into a *streaky*[1] pattern (confirming the removal of the oxide) the temperature is ramped down to the growth temperature; the growth is then started by opening the In shutter. For this experiment the sample is exactly in the Bragg condition for the $[1\,0\,1\,.\,5]_s$. The exact position of the WZ Bragg's peak is determined using previous test experiments, since the sample is at high temperature and thus the lattice constant.

Once the growth is started the Bragg's peak intensities are recorded for one full growth of approximately 2 hours. Then the In flux is turned off and the sample is cooled down under As flux, until the substrate temperature reaches approximately 250 °C.

3.2.1 Results

The evolution of the WZ and ZB Bragg's peak intensity is measured by summing the intensity of every pixel inside the ROIs reported in figure 3.2.

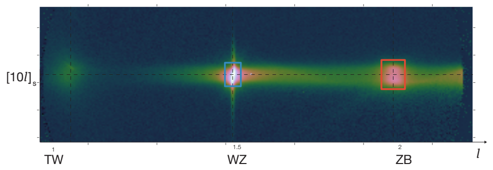

Figure 3.2: Characteristic Pilatus detector image showing the region of interest for the study of nanowire growth dynamics. The light blue and red ROIs are used to monitor the evolution of the WZ and ZB Bragg's peak intensity respectively.

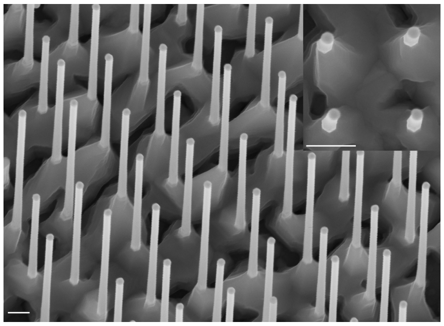

Figure 3.3: Representative SEM micrograph of NW array. The NWs have the same morphology as highlighted in the inset on the top right. Main image taken at 10°of tilting, inset at 2 °; the scale bars are 200 nm in both images.

Ex-situ high-resolution TEM studies show that the NWs have a pure WZ structure. Moreover SEM studies show that the nanowire arrays have an very uniform morphology across the whole sample and extensive parasitic growth in between the nanowires; as an example a SEM micrograph is reported in figure 3.3. In figure 3.4 the evolution of the WZ and ZB peaks is reported. Considering the result of the ex-situ microscopy analysis we associate the WZ Bragg peak intensity evolution only to the NW growth and the ZB only to the parasitic growth on the substrate. From 3.4 a) it is possible to see the evolution of a complete growth. After a short time lag both WZ and ZB grow in a steady state regime, i.e. the slope of the intensity evolution is constant. After around 50 minutes of growth the signal from the nanowires suddenly stops

---

[1] The reader will excuse the colloquialism but without diving into the electron diffraction realm it's easy to grasp the meaning; a *streaky* pattern can only be generated by a crystalline surface, since RHEED is extremely surface sensitive even a thin layer of native oxide produces a diffuse reflection rather than a streaky pattern.

increasing, suggesting that the condition at the growth front have changed. It is reasonable to think that the high density of nanowires combined with their height is reducing the collection area and thus the wires are growing only from direct impingement of growth material on or very close to the droplet. Also a rough planar growth tends to decrease the diffusion length of adatoms, because they will have more available sites for incorporation in planar growth, as suggested also by the evolution of the ZB intensity reported in 3.4 a).

We also note the effect of the cool down after 2 hours: the intensity of both ZB and WZ decrease significantly. We tend to rule out desorption since the cool down is performed under As flux and thus the structures are stabilized. A better explanation is instead that the lattice constant of the crystal structure is changing with temperature thus moving both peaks out of the chosen ROIs.

Lastly in figure 3.4 b) a zoom on the beginning of the growth is reported. We see that there exists a time lag between opening the In shutter and the beginning of NWs growth. A malfunction or lag of the shutter is ruled out as the same effect is seen in other samples, albeit not reported in this thesis. The observed time lag is instead a feature of the VLS mechanism of growth and is referred to as incubation time[8, 23]. Kalache et al. [23] explains the origin of the incubation time, albeit for Au-assited Si nanowires, as the time required for Si to diffuse through the Au particle thus reaching a regime where nucleation can start at the solid liquid interface; the authors pay no attention to the actual nucleation kinetics, which we instead think are extremely relevant. Consonni et al. [8] use standard island nucleation theory, where the incubation time follows Arrhenius dependency, to determine both the critical nucleus size and the activation energy of the nucleation process. In light of the formalism presented in 1.5 we think that using an Arrhenius dependence may be not enough because of the interplay of diffusion on the substrate, impinging beam fluxes, liquid diffusion and nucleation. We determine the incubation time to be 15 seconds for the sample shown in figure 3.4. More growths are performed varying both the growth the temperature at a fixed $\frac{V}{III}$ ratio and the $\frac{V}{III}$ ratio at a fixed growth temperature with the aim to understand the effect of the growth parameters on this aspect dynamics of NWs growth. At the time of writing the analysis are still in the preliminary stage and thus not included on this thesis.

By slicing the detector image along the growth direction, and summing over the the k direction, (cf. figure 1.11a) one can monitor the overall axial dynamics of the growth. In figure 3.5 such a measurement is shown; the derivative of the overall scattered intensity is plotted as function of the out of plane, i.e. along the growth direction, momentum transfer vector (labeled as Q_z) and time. Several interesting features emerge. As clear from figure 3.5a) around the WZ peak Laue fringes are visible. This can also be seen in figure 3.5b) where line cuts at representative times are reported. It's easy to see that period of the oscillations gets smaller suggesting that *something* in real space is getting bigger, moreover we can deduce that the distribution of the dimension getting bigger is uniform across the whole sample, else the oscillations would cancel out. Considering we are looking at the out of plane scattering vector we conclude that the nanowires length is the culprit of the oscillations. As seen in figure 3.5a) for a growth time greater that 300 seconds the oscillations seem to disappear. Two factors contribute to this; first, while at the beginning the nanowires are very short (0-20 unit cells) and the distribution contains a limited number of possible lengths, at a later stage the nanowires are longer with a much broader distributions of possible lengths thus *smoothing out* the fringes. Second, as the nanowires grow the oscillations have smaller periods, reaching a such small value in ΔQ_z that it falls below the resolution of the detector i.e. one period is smaller that one pixel. To get a feeling of this behavior one can set up a very simple model. If we consider that, at the very beginning of the growth, nanowires are linearly distributed with length varying from 0 to L unit cells and at time t-1 between 0 and $L-1$ then we can write

$$F_L(\mathbf{Q}) \propto= \sum_{l=0}^{L}\sum_{j=0}^{l} e^{i\mathbf{Q}\cdot\mathbf{R}_j} = \sum_{l=0}^{L-1}\sum_{j=0}^{l} e^{i\mathbf{Q}\cdot\mathbf{R}_J} + \sum_{j=0}^{L} e^{i\mathbf{Q}\cdot\mathbf{R}_j} \tag{3.1}$$

where the first summation takes into account the distribution of unit cells' lengths. The derivative can be written as:

$$F_L(\mathbf{Q}) - F_{L-1}(\mathbf{Q}) = \sum_{j=0}^{L} e^{i\mathbf{Q}\cdot R_j} \qquad (3.2)$$

which indeed gives fringes corresponding to nanowires of length L unit cells. To obtain quantitative information, such as the length of the nanowires and the growth rate, we fit a model similar to the one reported above, but allowing for a more realistic Gaussian distribution for the lengths of nanowires. At the time of writing we have found great agreement with the measured NWs length from the nanowires and the result of the fitting procedure, but the analysis are still in preliminary stage and thus are not reported in this thesis.

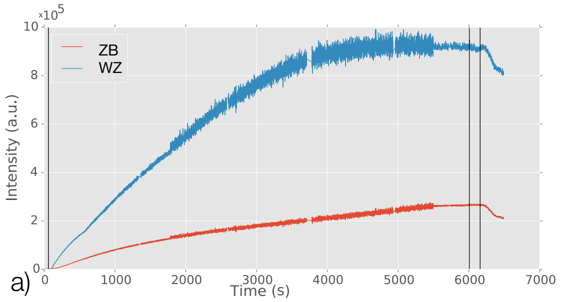

Figure 3.4: InAs nanowire growth dynamics overview. The WZ and ZB Bragg's peak intensities are calculated from the ROIs reported in figure 3.2. a) Overview of the full growth; the first vertical line shows when the In shutter was opened, thus starting the growth whereas the second line shows when the growth was halted by closing the In shutter, finally the third line shows when the cool down started. The sudden increases in the noise of the signal are due to the changes in the attenuation used during the measurement to avoid reaching saturation of the detector. b) Zoom in on the beginning of the growth, the first black line shows when the In shutter is opened and the dashed line, at time $t_i = 75$s econds, shows when the intensity of the WZ peak start increasing.

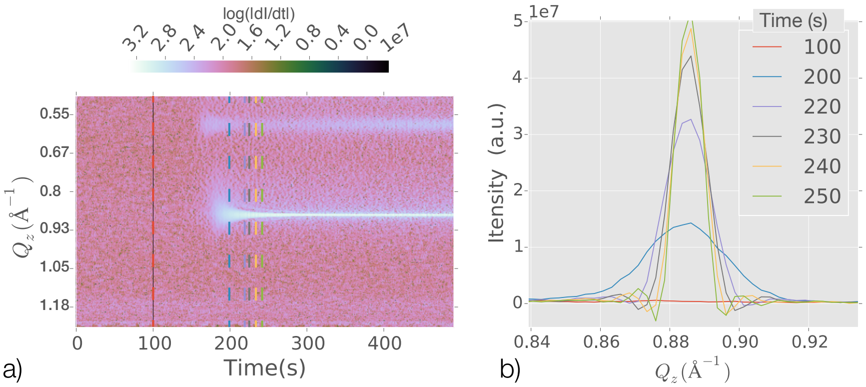

Figure 3.5: Laue oscillations in the growth direction. a) Logarithm of the absolute value of the derivative of the intensity as function of out of plane scattering vector and time. Oscillations are easy to see around the WZ peak at $Q_Z = 0.89^{-1}$. b) Line cuts to highlight the decreasing period of the Laue oscillations as the growth time increase. Traces are color-coded with the dotted line in a) to highlight their position in time.

3.3 Growth interruptions

Growth interruptions, i.e. shutting off the In flux, are used in order to study dynamic effects that lead to changes in the crystal structure. The growth interruption method has been already reported as a tool to grow ZB/TW/WZ superlattices, [5, 14] but the dynamics of the changes of crystal structure are in general lost when performing ex-situ measurements making it harder to understand the evolution of the system. The substrates for the nanowire growth were prepared as explained in section 2.3.2; the design, a square 10mmx10mm array with a 2 μm pitch sketched in figure 3.6 guarantees that the X-ray signal is coming from the nanowires (the sample is aligned so that the X-ray beam hits at the center).

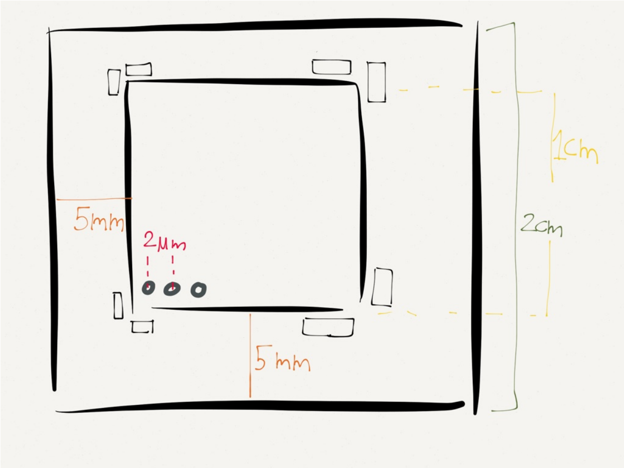

Figure 3.6: Substrate Design

The substrates are annealed at 530° C to desorb the native oxide. RHEED in this case is not used as the surface is covered with SiO_2 and thus would not give any valuable information. Nanowires are grown for 30 minutes with the growth parameters established to give the best results after several test growths (T_{pyro} = 400 °C, T_{in}= 850 °C, As flux = 3.17×10^{-4}). After 30 minutes the In shutter is periodically opened and closed.

3.3.1 Results

In figure 3.7 a characteristic Pilatus detector image is reported. It is easy to see both the TW and WZ peaks and their CTRs. To follow the time evolution of a certain crystal structure we select a region of interest (ROI) and then plot the sum of every pixel inside the ROI intensity as a function of time as shown in figure 3.8.

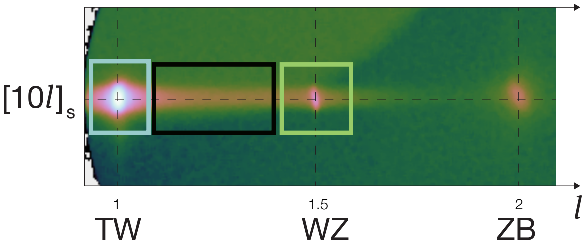

Figure 3.7: Characteristic Pilatus detector image showing the region of interest for the study of nanowire growth dynamics. The green, black and baby blue ROIs are used to study the evolution of the WZ, TW and CTRs scattered intensities.

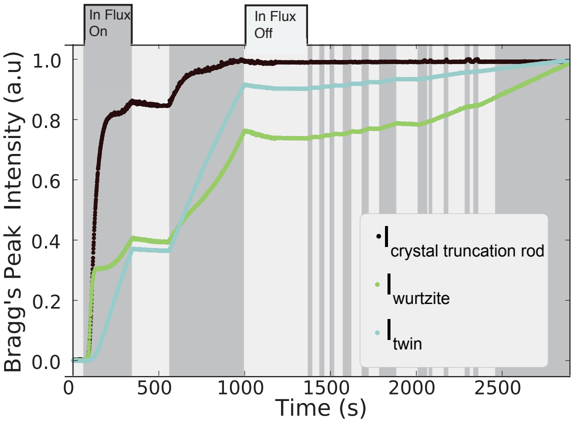

Figure 3.8: Normalized intensity of the different crystal structures Bragg's peaks for one full growth; the In beam flux is open in darker shaded regions and closed in the light regions.

It immediately jumps to the eye that at the very beginning of the growth the WZ peak's intensity seems to increase very fast and then suddenly stops increasing, as if the nanowires were growing at a very high growth rate at the beginning and then suddenly slow down. Although this effect looks interesting and possibly related to the nanowire growth dynamics we tend instead to rule out that it's only a dynamical effect. It's much more probable that it's related to the relative position of the detector/Bragg peak/CTRs. Even though the sample aligned close to the Bragg condition for $[1\,0\,1\,.\,5]_s$, we are also measuring at an high temperature and so the lattice constant increases, thus moving further away from Bragg condition. Also the WZ Bragg peak does not exist on the sample before growth, so it's not possible to align the set-up with it. Considering all above, the very beginning of the growth requires further analysis and it was not examined in depth in this project.

From post growth SEM and TEM imaging we can conclude that the NWs obtained from a given sample have the same overall morphology, similar faceting and crystal structure distribution, as an example representative SEM micrograph of an array of nanowires is reported in figure 3.9.

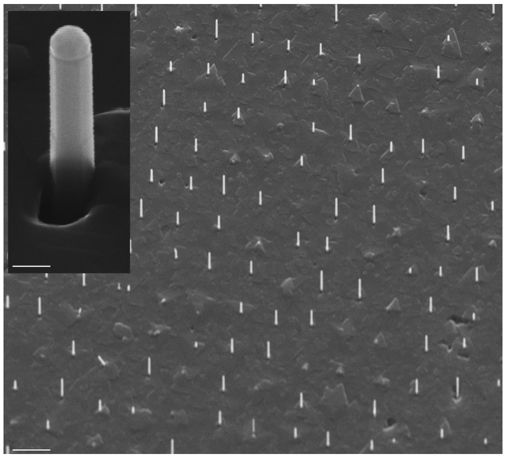

Figure 3.9: Representative SEM micrograph of NWs array grown; the nanowires are mostly uniform, and have the same morphology as the one reported in the top left inlet. The scale bar is 2 μm for the overview and 100 nm for the inlet.

Let's now focus on the later stage of the growth. High-resolution TEM and scanning transmission electron microscopy (STEM) studies show that the NWs have a pure WZ structure separated with thin slabs of ZB at the same locations relative to the NW length. An example is reported in figure 3.12. We can correlate these structural changes to the growth interruptions made during growth, where the In shutter was opened and closed. The five structural changes highlighted in figure 3.12 are the effect of the 5 on/off cycles reported in figure 3.13.

During steady state growth conditions we can see that the NWs form a pure WZ phase, while the measured dynamics in the non-steady state growth regime, which is induced by opening and closing for the In flux, show abrupt changes in the crystal structure. In fact, there exists a certain growth regime that promotes WZ to ZB reconstruction transitions. This regime seems to require a certain stage in growth, as the reconstruction transitions are measured only in certain periods. This behavior indicates that the growth interface morphology plays a crucial role in the resulting crystal structure during growth, as suggested previously[28, 29]. We also found that the length of the growth interruption influence the height of the slabs.

In figure 3.13 b) the intensity evolution of the ROIs highlighted in 3.13 a) is shown. Although it is not possible to categorically distinguish between the TW signal coming from the substrate parasitic growth and the signal coming from the slabs in the nanowires we believe that the signal is indeed coming from the nanowires due to the striking anticorrelation of the intensity of TW and WZ; the latter can only be a signal from the nanowire, as to the best of my knowledge no bulk InAs WZ structure has ever been found. Such an anticorrelation can be explained by crystal reconstruction meaning that for a certain state of the growth front it is favorable to nucleate in the ZB structure (either as an island in the top facet, or on the TL [15, 30]) thus introducing partial dislocations; partial dislocations can then glide under the driving force of a decrease in cohesive energy [2] inducting a solid-solid ZB to WZ structural transition. Although with our measurement we can not follow such a process at the required detail,

---

[2] As mentioned in section 1 it is known that ZB has a lower, although measured only in bulk, cohesive energy.

i.e. at atomic level, Zheng et al. [45] reported the same findings using in situ TEM analysis.

We now need to turn our attention to the nucleation of ZB at a certain configuration of the growth front, as proposed by Krogstrup et al. [28]. It can be shown, using equation 1.40 that for the same liquid supersaturation the probability of nucleating ZB(WZ) is:

$$P_{ZB(WZ)} \propto \int_0^{30_\circ} e^{-c(\omega)\frac{\Gamma^2(\omega)}{\Delta\mu_{ZB(WZ)}k_bT}}\, d\omega \tag{3.3}$$

where $\frac{\Gamma^2(\omega)}{\Delta\mu_{ZB(WZ)}} = \Delta G^*$ i.e. the maximum the free energy upon nucleation, $\Gamma(\omega)$is the effective surface energy of the nucleus , $c(\omega)$ is the nucleus shape factor, ω is the angle between the center of the nanowire facet and the site where the nucleation event takes place, as shown in 3.10. The integration limits reflect the six fold symmetry of the nanowire.

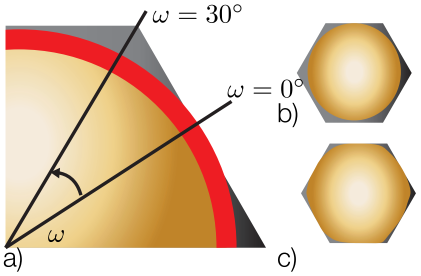

Figure 3.10: Droplet-NW configuration on the top-facet. a)Nucleation sites on the top facet, the red line represent the TL. b) An axis-symmetric droplet. c) A six-fold symmetric droplet with a TL pinned at the side facet of the nanowire.

We can see that $\Delta\mu_{ZB(WZ)}$ is the driving force towards nucleation of ZB(WZ) at a given droplet size/shape. So to understand the effect of the droplet shape on the crystal structure we need to see how $\Gamma^2(\omega)$ and $c(\omega)$ change with the the shape of the droplet. Using equation 1.28:

$$\frac{d}{dt}N_l = I_{III} + I_V - I_{inc}. \tag{3.4}$$

and considering that evaporation of group III elements is negligible at the growth temperature in use[28], the opposite being true for evaporation of group V, we can write:

$$\frac{d}{dt}N_l = I_{III} - I_{III,l-a} - I_{inc}. \tag{3.5}$$

where I_{III} is the liquid sorption current for group III elements, $I_{III,l-a}$ is the liquid to adatom flux. Equation 3.5 means that the volume changes are due to a change in group III, and that the amount of group V in the liquid is low. As seen in equation 1.38 the liquid to adatom flux depends on the concentration in the liquid, however we now experimentally that $I_{III} > I_{III,l-a}$, meaning that more group III gets sorbed into the droplet than group III elements go from the liquid to the adatom phase. We also know that I_{inc} increases with I_V because one group V atom takes one group III to form a pair and precipitate into the solid phase. From equation 3.5 we can conclude that a higher (lower) $\frac{V}{III}$ ratio (i.e. $\frac{I_V}{I_{III}}$) makes the volume of the droplet to decrease (increase). The effective surface energy of the nucleus can be written as[28]:

$$\begin{aligned}\Gamma^2(\omega) = &\Big[1 - \alpha(\omega) - \beta(\omega)\Big]\gamma_{sl-step}\\ &+ \alpha(\omega)\Big[\gamma_{sv,ZB(WZ)} - \gamma_{lv}sin(\theta(\omega))\Big]\\ &+ \beta(\omega)\Big[\gamma_{sv-step} - \gamma_{lv}sin(\theta(\omega))\Big]\end{aligned} \tag{3.6}$$

where $\gamma_{sl-step}$ is the solid step-liquid energy and γ_{lv}, $\gamma_{sv,ZB(WZ)}$,$\gamma_{sv-step}$ are the solid step-vapor side facet energy, liquid vapor surface, ans solid step-vapor energy respectively. $\theta(\omega)$ is the contact angle of the droplet with respect to the top facet, $\alpha(\omega)$ and $\beta(\omega)$ are the liquid free fractions of the nucleus perimeter in contact either with the side-facet or with the the top-facet of the nanowire respectively. Analyzing in details the different energies involved is beyond the scope of this experiment but we can group the relevant parameters (i.e. those that depend on the size of the droplet)[28] into: the fraction of the TL in contact with the side facet χ and the contact angle of the droplet with respect to the top facet $\theta(\omega)$.

As shown in [28] there exist two different scenarios: the droplet is small enough to be an axis-symmetric spherical cap with a circular TL as show in figure 3.10 b), the droplet is bigger and parts of the TL are pinned at the side-faces of the nanowries and the TL is no longer circular but has the shape of an hexagon, as show in figure 3.10 c). In the first case χ is equal to zero for all the values of ω and the contact angle is equal to the equilibrium wetting angle, $\theta(\omega) = \phi \quad \forall \quad \omega$. In the latter case $\theta(\omega)$ changes continuously along the TL and it has the biggest value at $\omega = 0°$ i.e. when in contact with the sidefacet and the lowest value when $\omega = 30°$, as shown in figure 3.10 a). The the fraction of the TL in contact with the side facet, χ, must be evaluated numerically by simulating the evolution of the shape of the droplet. As calculated by Krogstrup et al. [28] there exist two regimes (cf.1.5). If $\theta(\omega = 0) < 90°$ (i.e. the droplet is smaller or equals to half a sphere with the same radius of the NW, figure 3.11b) then the growth proceeds in regime I and an increase in the droplet size will favor the formation of WZ because the sin($\theta(\omega)$) is increased in 3.6. On the other hand if $\theta(\omega = 0) > 90°$, as shown in figure 3.11c, the $sin(\theta(\omega)$ is decreased in 3.6 thus favoring the formation of ZB. In conclusion below a certain $\theta = \theta_c$ a decrease in $\frac{V}{III}$ ratio makes the droplet bigger and thus χ bigger, favoring the formation of WZ. Above the θ_c the opposite holds true until the TL expands onto the sidefacet and the growth proceeds in regime II, as shown figure 3.11d. During regime II, calculating the most probable crystal structure is rather complex, but it can result either into nanwoire tapering or kinking [26, 28].

We can now interpret the data reported in figure 3.13. The nanowires grow in the WZ structure due to the selected $\frac{V}{III}$ ratio, where one can assume that the droplet is big and the wetting angle is low (TL still pinned to facets); whenever the In shutter is closed the $\frac{V}{III}$ ratio gets bigger and the TL retracts and is in contact only with the top facet favoring the nucleation of ZB. The droplet can also be big enough during growth that, even though the In shutter is closed, the WZ structure is still the favored crystal structure, and this explains why we see the WZ-TW transition only at certain stage of the growth. We also note that the In flux could decrease gradually during growth, primarily due to a smaller adatom collection (cf. section 1.5) but also due to experimental factors (i.e. In cell giving a less intense beam flux at the given temperature over time) which makes even more evident why the transitions only happen at a later stage of the growth (i.e. when the droplet is in the *small enough* regime).

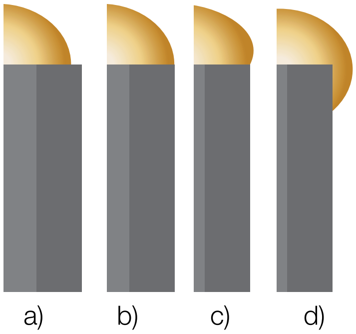

Figure 3.11: Droplet-NW configuration on the side-facet. a) b) c) are different configuration for the growth regime I, whereas d) is growth regime II. a) The TL is in contact only with the top facet. b) The droplet is bigger with respect to a) but the contact angle is lower than $90°$. c) The volume keeps increasing and the contact angle is greater than $90°$. d) The TL is no longer only in contact with the top facet but extends over the side facet.

The deposited SiO_2 film on the substrates presents epitaxial growth but still parasitic growth spreading from the root of the nanowires is observed suggesting that a better family of substrates for in-situ studies could be silicon $(1\,1\,1)$ with SiO_2 oxide film though the growth of InAs NWs on this kind of substrates is still far from being optimized.

Nonetheless the parasitic growth crystal structure is characterized with reciprocal space maps and is found to be composed of slabs of varying thicknesses, increasing with growth time, with high symmetry facets, mostly $\{1\,1\,\bar{1}\}$ and $\{3\,1\,\bar{1}\}$, as shown in figure 3.14 a) and schematically illustrated in 3.14 b). The time derivative of the scattered intensity dI/dt corresponds to the instantaneous growth rate and can be used to identify changes in growth of different structures. Laue fringes are observed next to the TW and ZB peaks as reported in figure 3.14 c) in the dI/dt signal, meaning that the substrate growth takes place forming slabs of the uniform thickness in the measured area. Moreover, the frequency of the fringes increases in time, suggesting that the linear growth rate (ML/s) increases, whereas the volumetric growth rate stays constant. This is possible in case of the pyramid formation, where thicker slabs grow at the top in order to conserve the volume.

In conclusion we have studied the dynamics of the growth of nanowires and parasitic growth separately, thanks to the oxide layer deposited on the substrates. We find out that it is possible to create abrupt crystal phase changes in InAs NWs by solid phase reconstruction transitions.

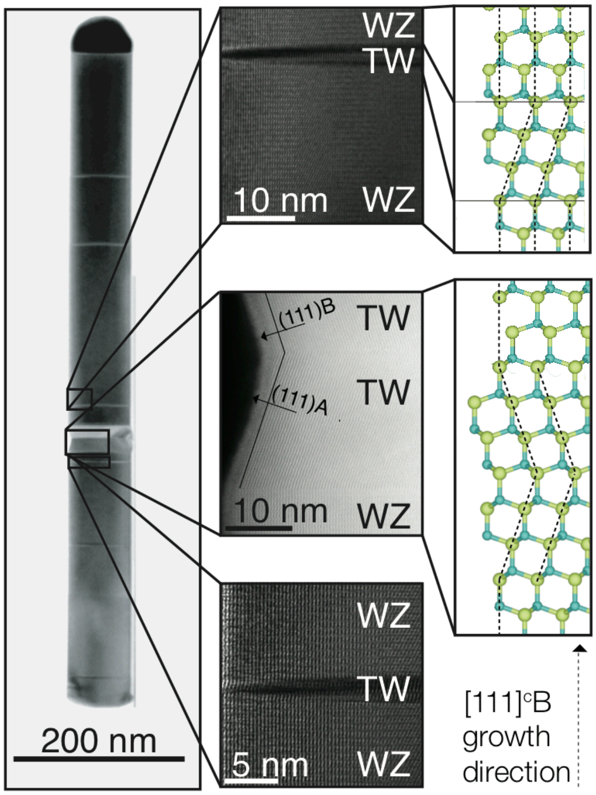

Figure 3.12: An example of a TEM images of a NW from the growth experiment. More TEM images are taken and they all show the same morphology. Central insets, top and bottom: HRTEM showing the sharp interfaces created by the formation of a thin TW slab. Middle inset: STEM image of the neck region of the nanowire where a sharp transition from WZ to TW and formation of twinned TW is noticeable. The reported phase changes are correlated with the five opening/closing the indium flux reported in 3.13. Right insets, crystal structure models of the central inset figures.

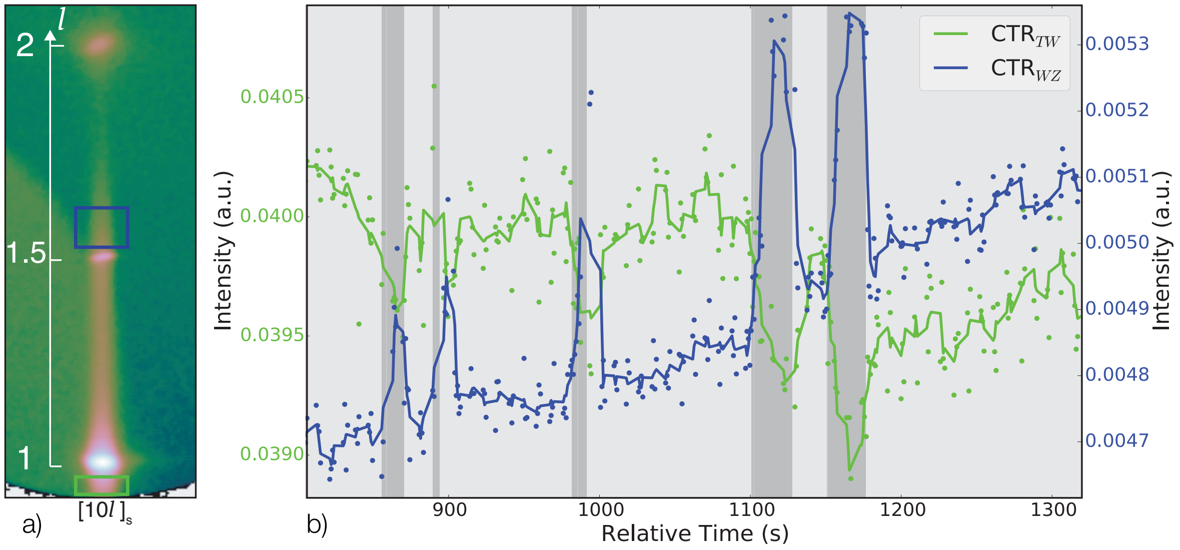

Figure 3.13: Reciprocal space model overlaid to a snapshot of the actual recorded data (time 800s). Miller Indices follow the surface-index notation. b) CTR intensities from the marked regions in a) as a function of growth time for a selected growth period. In flux is on during in darker shaded areas. The CTR intensities are proportional to the volume of the thin slabs of the respective structures. The observed trend suggest that an increase in In pressure favors the formation of thin WZ slabs and ZB to WZ reconstruction, whereas for strong reduction (i.e. turning the flux off) the opposite holds true.

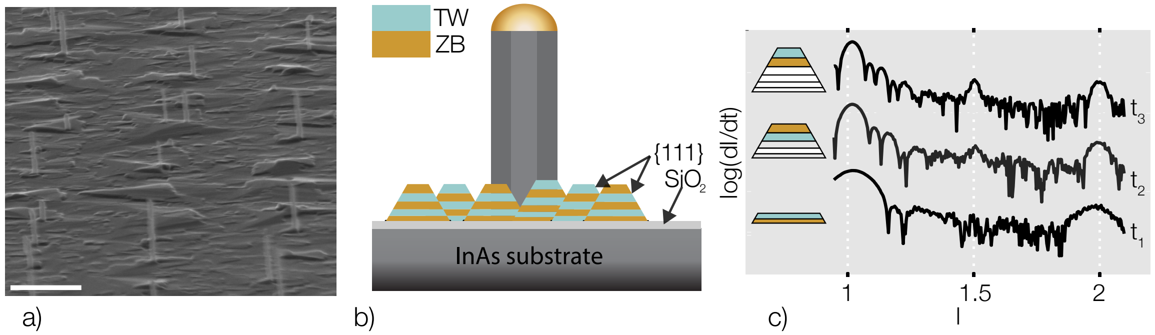

Figure 3.14: a)SEM micrograph showing the parastic growth morphology; the scale bar is 1 μ. b)Schematic diagrams showing the morphology of the parasitic substrate growth consisting of the pyramidal islands of ZB with multiple twin faults. c) Laue fringes next to the TW Bragg peak show increasing thickness of the TW/ZB slabs towards the top of the islands.The traces are taken at three different times ($t_1 < t_2 < t_3$) and are offset to highlight the different frequency of the Laue fringes.

4 | Conclusions and outlook

Conclusions

In **Chapter 2** we have shown that controlling the size of the catalyst particle required for growing nanowires with the VLS method can be done over a wide range and with high precision. Moreover we have shown that it is possible to control the position of the droplets with respect to the underling substrate's crystal structure. This result is one of the key ingredients for the formation of nanowire networks which will undoubtedly be of paramount importance in the future. We also show some preliminary and promising result for the formation of complex three dimensional architectures. Lastly we show that it is possible to produce substrate with an oxide coating to prevent undesired parasitic growth between nanowires. Such a family of substrates can be extremely valuable when performing in-situ studies, which provide a great amount of information on nanowire growth dynamics.

In **Chapter 3** we have reported the result from two beamtimes where we measured interesting effect of the NWs growth dynamics. From the first beamtime it has been shown that it is possible to create abrupt interfaces between different crystal structure along the nanowire axis. Also it has been show that the mechanism of the formation of such structures can be understood thanks to the formalism introduced in **Chapter 1**. These results highlight that nanowire growth is an extremely dynamical process. Lastly we show the the novel substrates fabricated play a significant role in altering the parasitic growth. From the second beamtime the incubation time has been measured for Au-assisted InAs nanowire growth; this was never observed nor measured before.

More measurements were performed during the second beam time such as: the determination of the incubation time for different combination of $\frac{V}{III}$ and temperature ratios, the measurement of the average instantaneous growth rate from Laue fringes in the growth direction, the dynamics of InAsSb and InSb axial shells on InAs stems. At the time of the writing the result from the second beam time are still in the preliminary stage so they have not been included in this thesis.

Outlook

One way to possibly improve the substrate fabrication is to use nano-imprint lithography[6] in lieu of the more traditional e-beam lithography. Such a change may improve the throughput and increase reproducibility but it may increase also the cost and reduce the flexibility of the design process because it requires the production of a mask. On the characterization side employing a last-generation atomic force microscope with a large scanning area could improve the precision of the measurement on the catalysts' size. Also one could think of using a grazing incidence X-ray technique and using the inherent averaging to have statistically correct information. In fact by using both wide angle and small angle scattering one could get both structural information and morphological information in one go. Although it mus be noted that with such a measurement getting the relevant information (size and shape for instance) can be much harder with respect to the technique used in this thesis, due to the modeling required.

To study the dynamics of NW growth one could also use the RHEED set-up on the MBE. Although it may suffer from more noise than an experiment at a synchrotron it definitely offers more flexibility. At present the set up at NBI is not equipped with the hardware or software required to perform time resolved measurements.

The ultimate goal would be to be able to perform a systematic in-situ study exploring in depth the dependence of the growth process with the all the possible conditions and coupling such measurements with dynamical simulations. While doing such studies may be quite hard because of the limited time-span of the beamtimes, coupling the already measured data with dynamical simulation is already in the pipeline of our research plan.

5 Acknowledgments

First and foremost I'd like to thank Jesper Nygård and Charlie Marcus for making my master project possible, without them I'd be still wandering around HCØsearching for an exciting journey into solid state physics. Without them I'd never had the chance to sit down and talk with Peter Krgostrup about the wonder of naowires; at that point I didn't know he would later become my supervisor, let alone such a wonderful supervisor. I had a great journey into the beauty of thermodynamics, and that's certainly due to Peter's great supervision all along.

Following no particular order, nor geographic nor chronological, let's start this show. A big thanks goes to the second floor crew. Merlin, thank you for stealing my wonderful plant and thus keeping it alive: in my horrible hands it would have certainly died. D204, aka the potential dwell in the corridor, has been a wonderful chilling spot for nice conversations and random 4pm beers and that's certainly due to the inhabitants of the office. Morten Kjærgaard, a kick-ass scientist and an overall awesome person, It's from your `oh man science is so f***** hard' still echoing in my brain that I often get over yet another failed exposure. Doctor Willy Chang, from you I have learned by osmosis so much science that not even two years of all day long book-devouring would have thought me. Also, without your taste for fine things this whole journey would have been oh-so-much duller. Looking forward to meet you again in Singapore, we still have a lot of Martini-Gin blends to try. Same goes for Andrew, an example I'd love to be able to follow in the future, when it comes to being an awesome person and awesome scientist: terrific combo! Sorry again for the heatgun, and thank you for reminding me that being mad at someone can be a good occasion to learn how to behave properly. My Italian friends, if I didn't have the wonderful time I had down there before leaving, I am sure I could not focus on science as much as I am doing now, still desperately searching for yet another afterpary. I can't deny I miss all the fun we had together. Having a somebody in-house to talk politics with has been a great pleasure, Johannes. I've learned a lot from our casual this-world-is-so-wrong conversations. Now that we both have some kind of job it's going to be immensely fun to plan cultural revolutions from posh cafes' and restaurants. Thorvald and Christian, the tricky act of balancing race-biking/eating/dirking together has been really awesome, stay assured that we will eventually beat professor Karsten. Also, don't despair, we will probably go trough the whole menu of cocktails and probably the whole set of spirits combinations at Oak Room soon with the oh-so awesome Wednesday night one-drink only tradition. Henri thank you for the quality time we spend together when working late at night, it's always nice to know that there is somebody else with a weird biorhythm and the same groovy music taste. Also, the high level programming and science related conversations, together with the staple let's go for the very-late night very-last cocktail have been a life saver. Jeppe and Shiv, thank your for tolerating my noisy keyboard and being awesome office mates when I started. I often miss having you in the office. Claus Sørensen, sometimes I wonder how it's possible to have such an immense technical knowledge. I have learned so much from your patient explanation on how *stuff* works; also thank you for being always there with all the MBE related tasks. Tomas Stakevic without your guidance I would still probably be lost somewhere in reciprocal space, working with you during the two beam times has been a true pleasure. Anders Jellinggaard without your casual awe-

someness and sharp suggestions I would not have ventured in fun challenge of learning yet another obscure programming language for the heck of it. Jess, Tina and Katrin thanks for being hands down the most amazing people ever. Without you everything in the lab would be so difficult if not impossible at times.

Lastly I am grateful to DNRF-DANSCATT for funding my two beamtimes in Japan, and to Danish National Research Foundation and Microsoft stationQ for funding most of the research and espressos at QDev.

Appendices

.1 Recipies

.1.1 Standard Substrate Recipe

Start with a full 2" inch InAs wafer open the sealed package only in the clean room and skip any kind of cleaning with organic solvents.

Resist spinning is performed as follow. For a small piece the best approach is to use a 10 ml plastic pipette, dunk it in the resist bottle staying away from the edges to avoid any contamination with the dried resist fibers sitting there. Mount the chip on the spinner, carefully try to match the geometrical center of the sample with the sample holder suction hole. When dispensing on the surface leave one single drop to touch the substrate and then keep a steady flow while in contact with the droplet. For a $\frac{1}{4}$ or bigger wafer use a 50 ml beaker with a *spout* instead of the pipette. Remember that resist is cheaper than the substrate and it's very important to cover the whole surface. Once the surface is covered, close the lid and start a spinning program that spins for 40 seconds at 4000 rpm. When the program is finished carefully transfer the wafer to the hot plate and back at 180 °C for 90 seconds. Baking time is not that important, whereas handling the wafer carefully is very important especially for big wafers as they are flexible and tend to snap. Let the wafer cool at least 20 seconds before spinning another layer, else you will successfully ruin the suction o-ring of the spinner. I have used for more at least a few hundreds of sample the following bilayer resist stack, in order of deposition:

- copolymer 6% i.e. co-MMA 6% in etil-lactate, commercial name EL6, from Microchem corp.
- polymer 2% PMMA 2% in in anisole, commercial name A2, from Microchem corp.

One is now faced with a choice: expose the full 2″, or cleave it in quarters, or even in smaller pieces. To each its own choice but if the wafer is cleaved in quarters make sure the they are as close as possible to geometrically perfect. A deviation greater than 1mm will make them not to fit in the MBE trolley. Considering the substrate is covered with the resist no significant dirt should be introduced no matter how dirty is the scriber or the surrounding environment. Although the scribing can be virtually done in every room, unless one really desires cancer, I'd suggest to have a ventilation system to remove the semiconductor particulate that is unavoidable when scribing.

Expose the chip according to the desired design. Depending on which the dose should be set accordingly. This implies that extensive dose testing must be performed and that there is no magic number that works all the time. Although a safe starting bet is to stay between 0.02, and 0.6 pC at 30 kV and between 0.1 and 8 pC at 100 kV, the numbers above depend also on the chosen aperture size. But in 90% of the scenarios they will produce dots.

Development is done with MIBK[1]:IPA , 1:3 (here after called PMMA developer) at room temperature. Time depends on the acceleration voltage, the optimal values I have found are 45 seconds for 30kV and 90 seconds for 100 Kv. A soon as the selected development time is over rinse the chip in ipa, and immediately blow dry with a nitrogen gun.

Before evaporating any metal ash for 20 seconds at 60 Watt in a microwave oven-oxygen plasma, with low oxygen[2].

Metal deposition is performed with a E-gun evaporator from AJA international at a base pressure of 10^{-8} torr. The suggested crucible for gold evaporation is an inter-metallic kind. Although it induces a noticeable slow down due to a long thermalisation process, it's the best way to avoid carbon contaminated gold.

Lift off is done with NMP[3] at 80 °C in a water bath. Usually the gold peels off nicely after two hours, and the major cause of bad or hard-lift off is overexposure during e-beam lithography. I use a two cups system where the first one is used for the first two hours, and the second one is kept at the same temperature but empty. When the gold looks completely peeled off the sample is dipped into the clean solution and then rinsed with acetone, and with IPA and quickly blown dry with a nitrogen gun.

Before loading into any MBE system, the substrate needs to be ashed again for 40 seconds and dipped

---

[1] Methyl isobutyl ketone

[2] actually in our lab it's mostly a nitrogen plasma due to a leak in the system

[3] N-Methyl-1-pyrrolidone

in a buffered 5% HF solution for 10 seconds.

Ion milling calibration

In figure 2 the results are reported where each point is the mean of different measurements and the errobar are the error on the mean.

Figure 1: Ion Milling parameters.

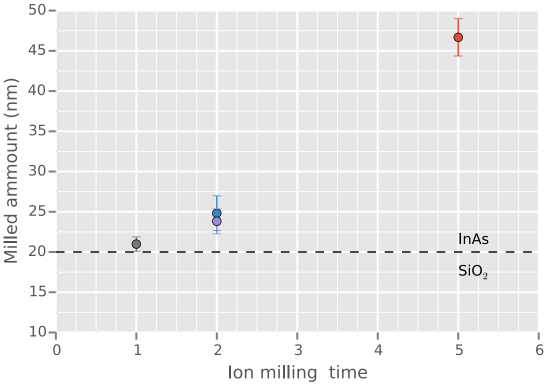

Figure 2: Ion Milling calibration results.

.2 Electron Matter Interaction

This section is partially adapted from a project I did before the master thesis.

When an electron beam hits a solid, multiple process are activated. The beam can be transmitted, depending on sample thickness, or it can be scattered due to interaction with the Coulomb field of both the sample electrons and nucleus. A graphical summary of the possible outcomes of the interactions is shown in figure 3, along with a qualitative positioning of their origin.

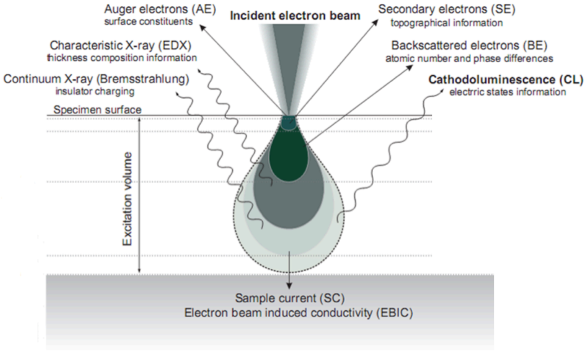

Figure 3: Electron matter interaction volume and signals generated.

In this project only backscattered electrons (BSE) and secondary electrons (SE) are used and thus other signals, although of vital importance for other applications, will not be discussed. It is worth noting that BSE and SE both contribute to image formation and to pattern exposure during lithography, the next paragraphs will describe their physical origin and properties.

As soon as an electron enters the solid it can either hit a nucleus or interact with the electron cloud-like distribution of the solid, the outcomes are really different: in the first case the collision will be *mostly* elastic whereas in the second case will be inelastic.
The first process is usually modeled following Rutherford backscattering theory and it is possible to say that the probability of being backscatter increases strongly with Z, the atomic number, approximately like $\propto Z^2$ and strongly decreases as the electron energy E increases approximately like $\propto \frac{1}{E^2}$, as it is possible to see in equation 1 [20]:

$$Q(>\phi_0) = k(\frac{Z^2}{E^2}cot^2(\phi_0)) \\ (events > \phi_0)/[electron(atom/cm^2)] \quad (1)$$

where Q is called the cross section (cm^2) for elastic scattering and it is the probability for scattering at an angle greater than ϕ_0, k is a numerical constant.

The second process is usually described like a continuos loss of electron energy due to small angle scattering events when the electron is traveling further down the solid. It was proposed by Everhart and Hoff [16] that the process can be modeled with the following equation, where the rate of energy loss, E, along the distance, S, is:

$$\frac{dE}{dS} = -2\pi e^4 N_0 \frac{\varrho Z}{E_i A} ln(\frac{1.116E}{J}) \quad (keV/cm) \tag{2}$$

where A is the atomic weight, J is the ionization potential, defined as the mean energy lost per collision, e is the electron charge, N_0 is the Avogadro number, ϱ is the density, Z is the atomic number and E_i is the electron energy at any point in the specimen.

Secondary electrons are loosely bound outer shell-electrons from the specimen atoms sitting in such a position that they get sufficient kinetic energy during inelastic scattering of the beam electrons to be ejected from the atom and set into motion. The SE can propagate through the solid, and some will intersect the surface and escape. Secondary electrons are defined mostly on the basis of their kinetic energy, and the threshold is empirically set to be $\approx 50eV$, any electron with greater energy is labeled as BSE instead.

Due to the mentioned scattering effect the depth of electron penetration is a function of the beam energy E_b [16]:

$$R_e = \frac{K}{\varrho} E_b^{\alpha} \tag{3}$$

where ϱ is the density of the material and k and α depend on the atomic weight of the material and on beam energy. An expansion to equation 3 is given by Kanaya and Okayama [24], and it is in greater accordance with experimental data for high atomic numbers and high beam energies:

$$R_e = \frac{0.0276A}{\varrho Z^{0.899}} E_b^{1.67} \quad (\mu m) \tag{4}$$

where A is the atomic weight in $\frac{g}{mol}$. Considering all the above models it is possible to understand that the electron-matter interaction is not spot-like but rather a volume-like interaction with a geometry that depends on the nature of the material and the beam energy. Usually *Monte Carlo*[4] simulations are done to estimate and visualize the size of the interaction volume.

Monte Carlo simulations are performed with the software CASINO version 3.2, a free tool often utilized for modeling electron matter interaction in literature [9]. By selecting the appropriate physical models, for the atomic numbers and beam energies in use, in this case the Kanaya and Okayama equation for the electron range and the Rutherford equation for the backscattering cross section, realistic approximations can be obtained. Figure 4 and 5 show the overview of the interaction volumes for two different energies 30 KeV and 100 KeV respectively. It is easy to visualize that both the depth and the width of the interaction volume are approximately one order of magnitude bigger for the high acceleration voltage. By zooming in a region close to the PMMA/InAs interface it is possible to visualize clearly the effect of both the BSE and inelastically scattered electrons. Due to the latter the beams gets noticeably broader by the end of the 200 nm resist for

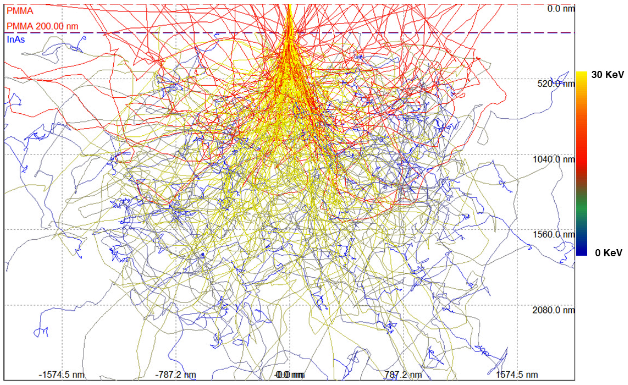

Figure 4: Overview of MC simulation for a 10nm 30 KeV electron beam , the colormap represents the energy of the electrons. The simulated sample consist of a 200nm thick PMMA resist and a bulk InAs substrate, 200 simulated electrons.

---

[4] *Monte Carlo methods (or Monte Carlo experiments) are a broad class of computational algorithms that rely on repeated random sampling to obtain numerical results i.e. by running simulations many times over in order to calculate those same probabilities heuristically*

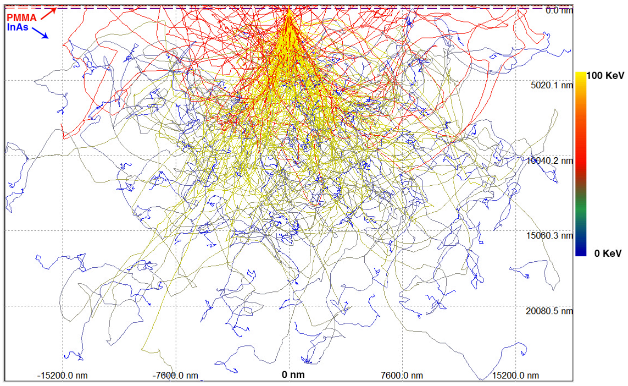

Figure 5: Overview of MC simulation for a 10nm 100 KeV electron beam, the colormap represents the energy of the electrons. The simulated sample consist of a 200nm thick PMMA resist and a bulk InAs substrate, 200 simulated electrons.

30 KeV (figure 6), whereas its it mostly constant for 100 KeV (figure 7). It is also worth noticing the amount of BSE about the beam axis is very high in a short range ($\approx$ 300nm) for 30 KeV whereas it is very low for 100 KeV, the opposite holds true in a long range ($\approx$ 10 μm). Lastly it must be noted that the above simulations give only a first approximation in understating the proximity effect, because they are considering just they only simulate 200 electrons, a non realistic dose in lithography.

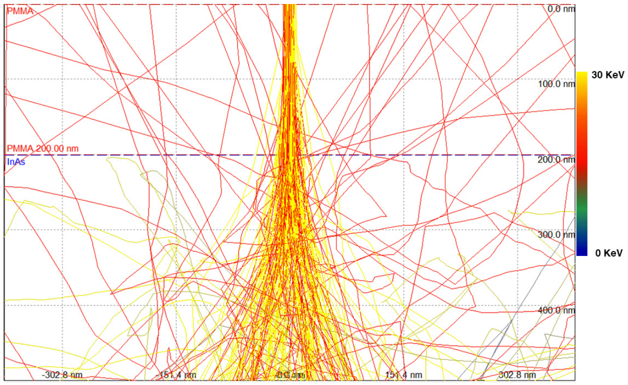

Figure 6: Zoom on the resist/semiconductor interface (500nm), same details as figure 4.

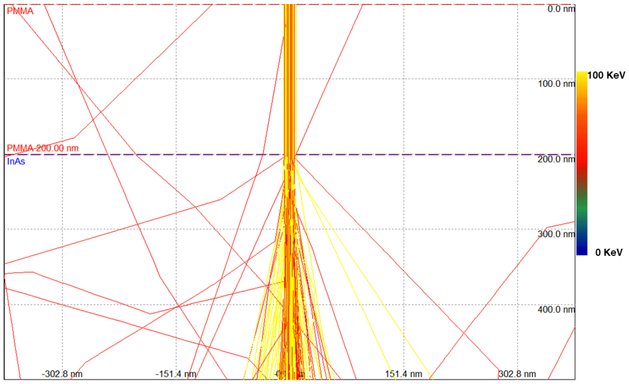

Figure 7: Zoom on the resist/semiconductor interface (500nm), same details as figure 5.

.3 Image analyis

I have developed an application to automatically measure the size of the dots from SEM pictures from our ZEISS SEM. It is optimized for speed and can easily crunch gigapixels. Using this software is possible to measure millions of dots and get proper statistics. The software is released under MIT license and variable on GitHub: https://github.com/giulioungaretti/qt_dot_fitter/. A brief explanation of the software follows.

To run the main app, app.py, exectute in one line:

```
python ./app.py ./path/reference_image.bmp ./path min_size format
```

where min_size is a gray number that limits the smallest possible are fitted by the app; there is no general rule, it must be found out iteratively and $format$ is the format of the images on the hard disk. There is an hidden last argument which comes in handy if working remotely and want to draw the GUI remotely and not over tunneled X11 on the local machine. The output of the fitted measurements is saved on the disk as .csv file for every image; use the helper functions in stat.py to parse the results and produce meaningful plots. The main GUI when opening the image is shown in figure 8.

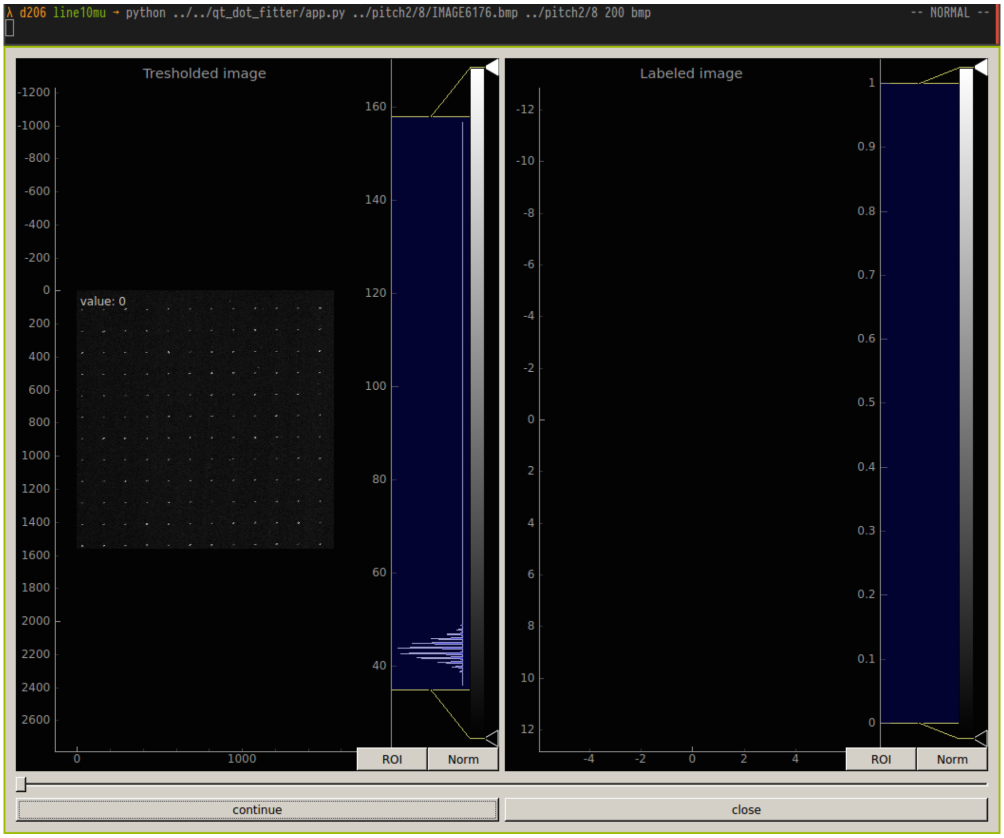

```
λ d206 line10mu → python ../../qt_dot_fitter/app.py ../pitch2/8/IMAGE6176.bmp ../pitch2/8 200 bmp                -- NORMAL --
```

Figure 8: Interface when opening the first reference file

The raw image is labeled by connecting regions of an integer array. After the intensity threshold has been selected with the slider to separate the contribution from the substrates and the geometrical dots (brighter). Two pixels are connected when they are neighbors and have the same value. They can be neighbors either in a 4- or 8-connected sense:

```
4-connectivity      8-connectivity

     [ ]           [ ]  [ ]  [ ]
      |               \  |  /
[ ]--[ ]--[ ]      [ ]--[ ]--[ ]
      |               /  |  \
     [ ]           [ ]  [ ]  [ ]
```

The algorithm will expand the connected pixel area until the connection dies, which basically means connecting the bright pixel of the dots we want to measure. As soon as the slider is moved the right panel will update with the labeled image to help choosing the correct threshold, as shown in figure 9.

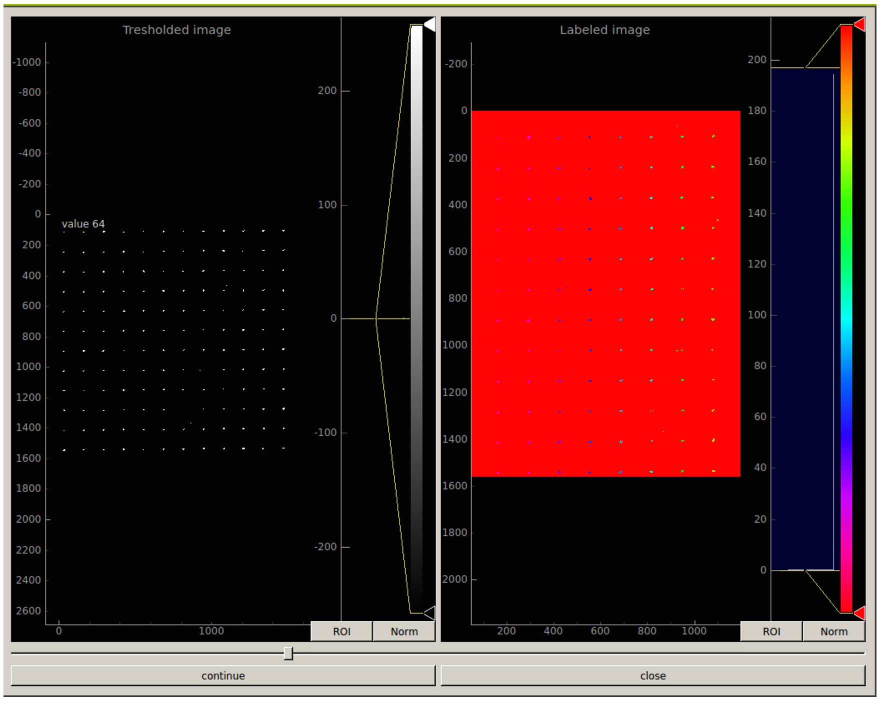

Figure 9: Labeled image. Different colors on the right side image mean different labeled regions

To close the program click *close*, to start the fitting procedure press *continue*. Ellipses are fitted to the features, i.e. the labeled areas of the image, to account for stigmation while writing and taking the images. The results of the fitting is plotted live in an external window, by superimposing a circle with a radius which is the average of the ellipses radii, an example result is reported in figure 10.

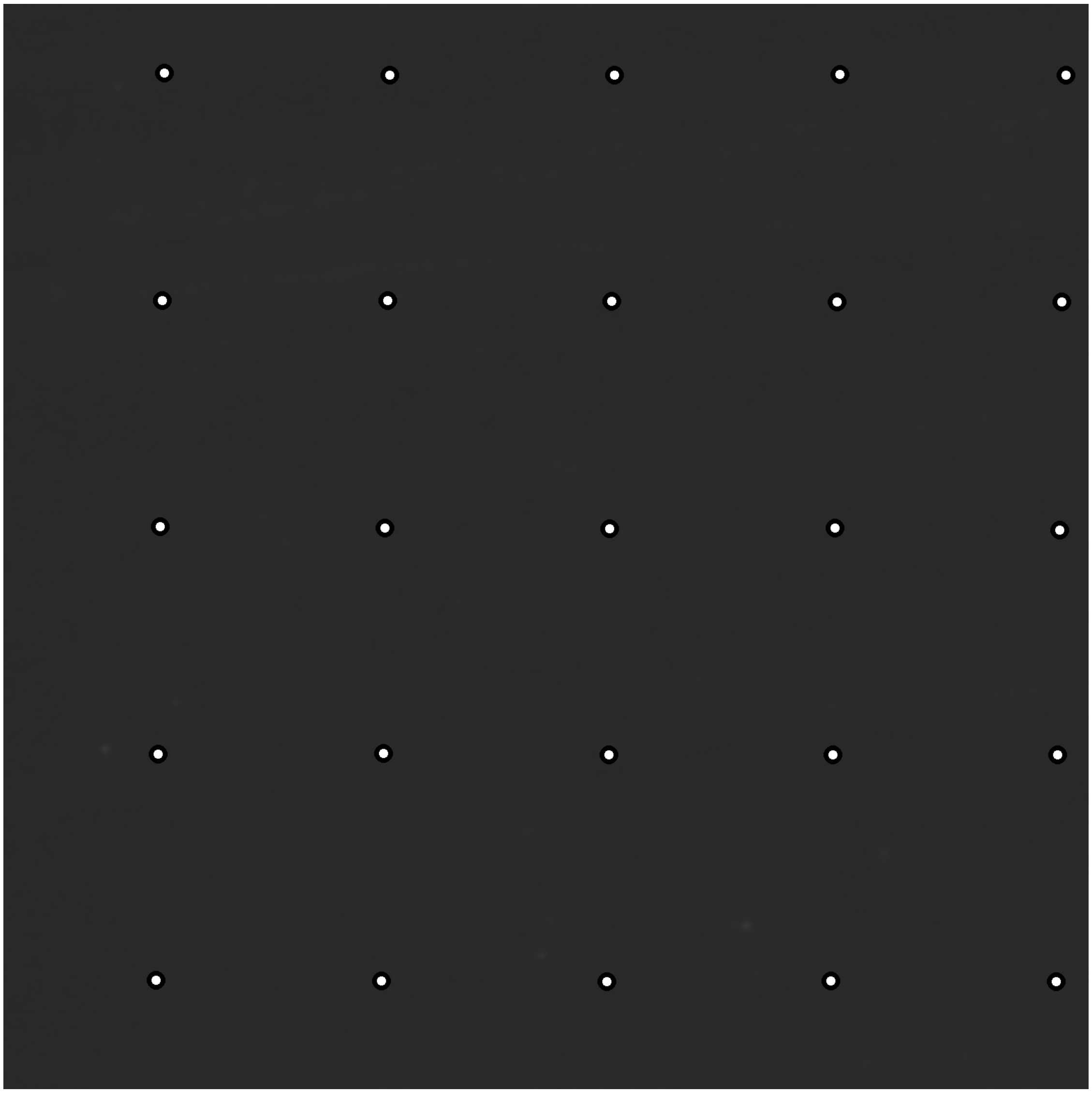

Figure 10: An example of the fitting results.

.4 X-ray data anaylsis

This code is meant to make analysis of X-ray data from in situ X-ray experiments at the SPring8 bl11xu, the source code is avaialbe at: https://github.com/giulioungaretti/SP2014.

file organization The idea here is to organize each sample's data in one folder; since we usually take multiple measurements and test measurements on each folder we create an array of subfolders with the same base name as the data they contain.

a note on performances Non nix based operating systems may have troubles managing high number of files, so this file organization will also prevent undesired crashes.

How to use the code

parse.py This code is responsible for the actual parsing of the images from the detector. It's assumed that they are .tiff files.

All the function and classes used in this script are defined in the `sp2014a.py` module (refer to the docstrings for more documentation).

The script will:

- load the images
- perform 3x3 median filter to remove any possible dead pixel
- load the flatfield images
- correct for signal background (using empty areas from the detector image)
- extract the time from the headers and covert to UNIX EPOCH time
- dump the times and images to disk with the agile hdf5 file format

example From a terminal that contains the folder named `sample` with `subfolders` named `sampled_mesasurement` and that contains a folder containing the flatfields measurements named flatfield

```
python parse.py sample/sample_mesasurement flatfield
```

The output of the program will tell you what's going on and throw an error if the files exist already.

dock.py This scripts generate as QT graphical user interface that shows the dector image as a function of time, and offers user movable region of interest (ROI) to visualize the time evolution of the intensity in that region. The scrpit will also dump a pandas dataframe containing the following informations:

- center of mass yellow ROI - FWHM (hk, and l directions) orange ROI - intensities of red ROI and green ROI

eample First run app.py inside an ipython shell for every scan recorded. Adjust the rois and save them to disk (for reproducibility, use the function `dumpd_roi` and `load_roi`.

```
%run dock.py name_of_sample # i.e sample/sample_mesasurement
```

attenuation correction.py Lastly we want to stich together all time different measurements for one sample and correct for attenuation changes. The latter is done manually by selecting the two end points that contain the moment where the attenuation was changed and using their ration to correct the remaining data. This has to be done for every attenuation change. The resulting corrected data is dumped to disk, and plotted. For simplicity this program must be run inside the sample folder.

```
cd ./sample
python attenuation_correction.py
```

plot.py This convenience script will load the dataframes with the data and plot the different data.

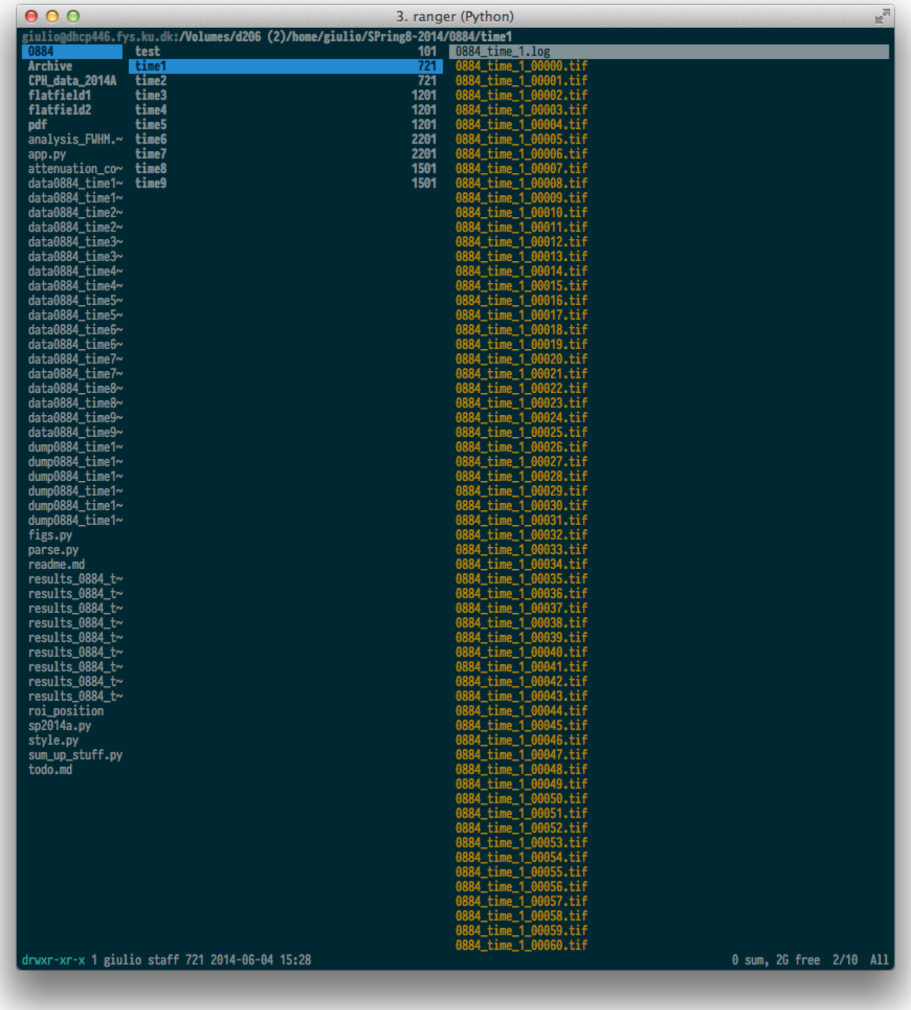

```
giulio@dhcp446.fys.ku.dk:/Volumes/d206 (2)/home/giulio/SPring8-2014/0884/time1
0884             test     101  0884_time_1.log
Archive          time1    721  0884_time_1_00000.tif
CPH_data_2014A   time2    721  0884_time_1_00001.tif
flatfield1       time3   1201  0884_time_1_00002.tif
flatfield2       time4   1201  0884_time_1_00003.tif
pdf              time5   1201  0884_time_1_00004.tif
analysis_FWHM.~  time6   2201  0884_time_1_00005.tif
app.py           time7   2201  0884_time_1_00006.tif
attenuation_co~  time8   1501  0884_time_1_00007.tif
data0884_time1~  time9   1501  0884_time_1_00008.tif
data0884_time1~                0884_time_1_00009.tif
data0884_time2~                0884_time_1_00010.tif
data0884_time2~                0884_time_1_00011.tif
data0884_time3~                0884_time_1_00012.tif
data0884_time3~                0884_time_1_00013.tif
data0884_time4~                0884_time_1_00014.tif
data0884_time4~                0884_time_1_00015.tif
data0884_time5~                0884_time_1_00016.tif
data0884_time5~                0884_time_1_00017.tif
data0884_time6~                0884_time_1_00018.tif
data0884_time6~                0884_time_1_00019.tif
data0884_time7~                0884_time_1_00020.tif
data0884_time7~                0884_time_1_00021.tif
data0884_time8~                0884_time_1_00022.tif
data0884_time8~                0884_time_1_00023.tif
data0884_time9~                0884_time_1_00024.tif
data0884_time9~                0884_time_1_00025.tif
dump0884_time1~                0884_time_1_00026.tif
dump0884_time1~                0884_time_1_00027.tif
dump0884_time1~                0884_time_1_00028.tif
dump0884_time1~                0884_time_1_00029.tif
dump0884_time1~                0884_time_1_00030.tif
dump0884_time1~                0884_time_1_00031.tif
figs.py                        0884_time_1_00032.tif
parse.py                       0884_time_1_00033.tif
readme.md                      0884_time_1_00034.tif
results_0884_t~                0884_time_1_00035.tif
results_0884_t~                0884_time_1_00036.tif
results_0884_t~                0884_time_1_00037.tif
results_0884_t~                0884_time_1_00038.tif
results_0884_t~                0884_time_1_00039.tif
results_0884_t~                0884_time_1_00040.tif
results_0884_t~                0884_time_1_00041.tif
results_0884_t~                0884_time_1_00042.tif
results_0884_t~                0884_time_1_00043.tif
roi_position                   0884_time_1_00044.tif
sp2014a.py                     0884_time_1_00045.tif
style.py                       0884_time_1_00046.tif
sum_up_stuff.py                0884_time_1_00047.tif
todo.md                        0884_time_1_00048.tif
                               0884_time_1_00049.tif
                               0884_time_1_00050.tif
                               0884_time_1_00051.tif
                               0884_time_1_00052.tif
                               0884_time_1_00053.tif
                               0884_time_1_00054.tif
                               0884_time_1_00055.tif
                               0884_time_1_00056.tif
                               0884_time_1_00057.tif
                               0884_time_1_00058.tif
                               0884_time_1_00059.tif
                               0884_time_1_00060.tif
drwxr-xr-x 1 giulio staff 721 2014-06-04 15:28          0 sum, 2G free  2/10  All
```

Figure 11: File organization example

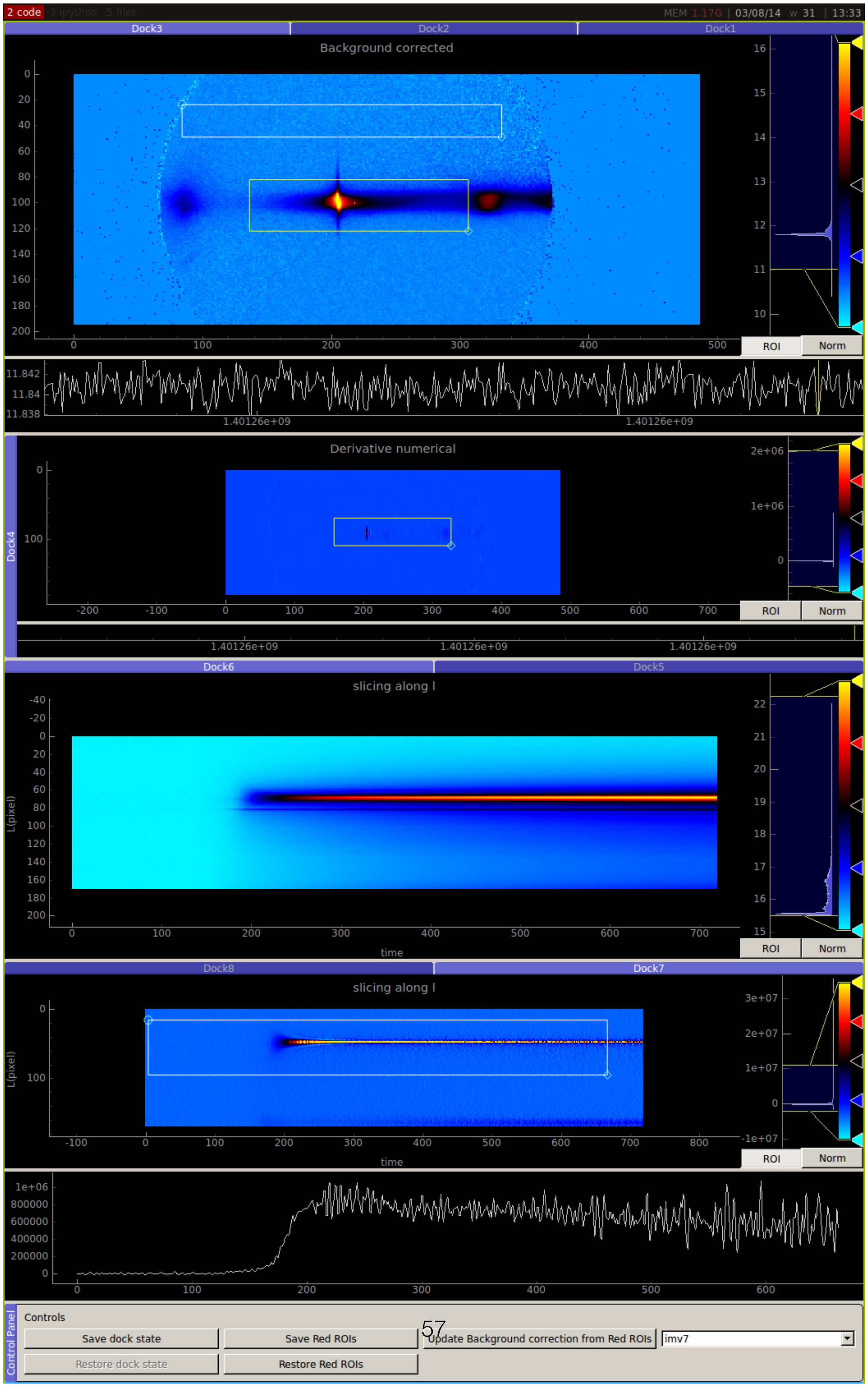

Figure 12: QT GUI

Nomenclature

BSE	Back Scattered Electrons
CTR	crystal truncation rod
ERS	equilibrium reference state
fcc	face centered cubic
LEED	low energy electron diffraction
MBE	molecular beam epitaxy
MIBK	Methyl Isobutyl Ketone
ML	monolayers
RHEED	reflection high energy diffraction
ROI	region of interest
SE	Secondary Electrons
SEM	scanning electron microscope
TL	triple line
TS	transition state
TW	twinned zinc blende
UHV	ultra high vacuum
VLS	vapor-solid-liquid
WZ	wurtzite
ZB	zinc blende

List of Figures

Bibliography

[1] Fabrication-university of leeds, 2014. URL `http://www.stoner.leeds.ac.uk/Research/TutFab`.

[2] J. Alicea, Y. Oreg, G. Refael, F. von Oppen, and M. P. A. Fisher. Non-Abelian statistics and topological quantum information processing in 1D wire networks. *Nature Physics*, 7(5):412--417, May 2011.

[3] N. W. Ashcroft and N. D. Mermin. *Solid state physics*. Saunders College, 1976.

[4] A. A. Balandin and K. L. Wang. *Handbook of Semiconductor Nanostructures and Nanodevices: Nanofabrication and nanoscale characterization*. American scientific publishers, 2006.

[5] J. Bolinsson, P. Caroff, B. Mandl, and K. A. Dick. Wurtzite-zincblende superlattices in InAs nanowires using a supply interruption method. *Nanotechnology*, 22(26), 2011.

[6] S. Y. Chou, P. R. Krauss, and P. J. Renstrom. Imprint lithography with 25-nanometer resolution. *Science*, 272(5258):85--87, 1996.

[7] Y. C. Chou, K. Hillerich, J. Tersoff, M. C. Reuter, K. A. Dick, and F. M. Ross. Atomic-Scale Variability and Control of III-V Nanowire Growth Kinetics. *Science*, 343(6168):281--284, Jan. 2014.

[8] V. Consonni, A. Trampert, L. Geelhaar, and H. Riechert. Physical origin of the incubation time of self-induced GaN nanowires. *Applied Physics Letters*, 99(3), 2011.

[9] H. Demers, N. Poirier-Demers, N. de Jonge, and D. Drouin. Three-Dimensional Electron Microscopy Simulation with the CASINO Monte Carlo Software. *Microscopy and Microanalysis*, 17(S2):612--613, July 2011.

[10] K. A. Dick and P. Caroff. Metal-seeded growth of III-V semiconductor nanowires: towards gold-free synthesis. *Nanoscale*, 6(6):3006--3021, 2014.

[11] K. A. Dick, K. Deppert, M. W. Larsson, T. Martensson, W. Seifert, L. R. Wallenberg, and L. Samuelson. Synthesis of branched 'nanotrees' by controlled seeding of multiple branching events. *Nature materials*, 3(6):380--384, June 2004.

[12] K. A. Dick, K. Deppert, T. Mårtensson, B. Mandl, L. Samuelson, and W. Seifert. Failure of the Vapor–Liquid–Solid Mechanism in Au-Assisted MOVPE Growth of InAs Nanowires. *Nano Letters*, 5(4): 761--764, Apr. 2005.

[13] K. A. Dick, K. Deppert, L. S. Karlsson, W. Seifert, L. R. Wallenberg, and L. Samuelson. Position-controlled interconnected InAs nanowire networks. *Nano Letters*, 6(12):2842--2847, 2006.

[14] K. A. Dick, C. Thelander, L. Samuelson, and P. Caroff. Crystal Phase Engineering in Single InAs Nanowires. *Nano Letters*, 10(9):3494--3499, Sept. 2010.

[15] V. G. Dubrovskii, N. V. Sibirev, J. C. Harmand, and F. Glas. Growth kinetics and crystal structure of semiconductor nanowires. *Physical Review B*, 78(23), Dec. 2008.

[16] T. E. Everhart. Determination of Kilovolt Electron Energy Dissipation vs Penetration Distance in Solid Materials. *Journal of Applied Physics*, 42(13):5837, 1971.

[17] R. Feidenhans'l. Surface-Structure Determination by X-Ray-Diffraction. *Surface Science Reports*, 10(3): 105--188, 1989.

[18] M. Galicka, M. Bukala, R. Buczko, and P. Kacman. Modelling the structure of GaAs and InAs nanowires. *Journal of Physics-Condensed Matter*, 20(45), 2008.

[19] F. Glas. Vapor fluxes on the apical droplet during nanowire growth by molecular beam epitaxy. *Physica Status Solidi B-Basic Solid State Physics*, 247(2):254--258, Feb. 2010.

[20] J. Goldstein. *Scanning Electron Microscopy and X-Ray Microanalysis*. Springer, 2003.

[21] C. Hammond. *The basics of crystallography and diffraction*. International Union of Crystallography Oxford University Press, Oxford New York, 1997.

[22] S. Hofmann, R. Sharma, C. T. Wirth, F. Cervantes-Sodi, C. Ducati, T. Kasama, R. E. Dunin-Borkowski, J. Drucker, P. Bennett, and J. Robertson. Ledge-flow-controlled catalyst interface dynamics during Si nanowire growth. *Nature materials*, 7(5):372--375, May 2008.

[23] B. Kalache, P. R. Cabarrocas, and A. F. Morral. Observation of incubation times in the nucleation of silicon nanowires obtained by the vapor-liquid-solid method. *Japanese Journal of Applied Physics Part 2-Letters & Express Letters*, 45(4-7):L190--L193, Feb. 2006.

[24] K. KANAYA and S. Okayama. Penetration and Energy-Loss Theory of Electrons in Solid Targets. *Journal of Physics D: Applied Physics*, 5(1):43--&, 1972.

[25] P. Krogstrup. *Growth and Characterization of Heterostructure Nanowires*. PhD thesis, University Of Copenhagen, June 2009.

[26] P. Krogstrup, J. Yamasaki, C. B. Sørensen, E. Johnson, J. B. Wagner, R. Pennington, M. Aagesen, N. Tanaka, and J. Nygård. Junctions in Axial III–V Heterostructure Nanowires Obtained via an Interchange of Group III Elements. *Nano Letters*, 9(11):3689--3693, Nov. 2009.

[27] P. Krogstrup, R. Popovitz-Biro, E. Johnson, M. H. Madsen, J. Nygård, and H. Shtrikman. Structural Phase Control in Self-Catalyzed Growth of GaAs Nanowires on Silicon (111). *Nano Letters*, 10(11):4475--4482, Nov. 2010.

[28] P. Krogstrup, S. Curiotto, E. Johnson, M. Aagesen, J. Nygård, and D. Chatain. Impact of the Liquid Phase Shape on the Structure of III-V Nanowires. *Physical Review Letters*, 106(12):125505, Mar. 2011.

[29] P. Krogstrup, M. H. Madsen, W. Hu, M. Kozu, Y. Nakata, J. Nygård, M. Takahasi, and R. Feidenhans'l. In-situ x-ray characterization of wurtzite formation in GaAs nanowires. *Applied Physics Letters*, 100(9), 2012.

[30] P. Krogstrup, H. I. Jørgensen, E. Johnson, M. H. Madsen, C. B. Sørensen, A. F. i. Morral, M. Aagesen, J. Nygård, and F. Glas. Advances in the theory of III–V nanowire growth dynamics. *Journal of Physics D: Applied Physics*, 46(31):313001, Aug. 2013.

[31] M. H. Madsen, P. Krogstrup, E. Johnson, S. Venkatesan, E. Muehlbauer, C. Scheu, C. B. Sørensen, and J. Nygård. Experimental determination of adatom diffusion lengths for growth of InAs nanowires. *Journal of Crystal Growth*, 364:16--22, 2013.

[32] S. O. Mariager. *X-ray Diraction from Semiconductor Nanowires*. PhD thesis, Nov. 2006.

[33] S. O. Mariager, C. B. Sørensen, M. Aagesen, J. Nygard, R. Feidenhans'l, and P. R. Willmott. Facet structure of GaAs nanowires grown by molecular beam epitaxy. *Applied Physics Letters*, 91(8), 2007.

[34] W. P. McCray. MBE deserves a place in the history books. *Nature Nanotechnology*, 2(5):259--261, May 2007.

[35] K. Momma and F. Izumi. VESTA 3 for three-dimensional visualization of crystal, volumetric and morphology data. *Journal of Applied Crystallography*, 44(6):1272--1276, Dec. 2011.

[36] H. Okamoto. In-O (Indium-Oxygen). *Journal of Phase Equilibria and Diffusion*, 28(6):591--592, Nov. 2007.

[37] M. Tchernycheva, L. Travers, G. Patriarche, F. Glas, J.-C. Harmand, G. E. Cirlin, and V. G. Dubrovskii. Au-assisted molecular beam epitaxy of InAs nanowires: Growth and theoretical analysis. *Journal of Applied Physics*, 102(9):094313, 2007.

[38] P. Terzieff, K. L. Komarek, and E. Wachtel. The Magnetic and Thermodynamic Properties of Liquid Au-in Alloys. *Journal of Physics F-Metal Physics*, 16(8):1071--1082, Aug. 1986.

[39] B. Van Heck, A. R. Akhmerov, F. Hassler, M. Burrello, and C. W. J. Beenakker. Coulomb-assisted braiding of Majorana fermions in a Josephson junction array. *New Journal of Physics*, 14(3):035019, Mar. 2012.

[40] R. S. Wagner and W. C. Ellis. Vapor-Liquid-Solid Mechanism of Single Crystal Growth. *Applied Physics Letters*, 4(5):89--&, 1964.

[41] D. Wang, F. Qian, C. Yang, Z. H. Zhong, and C. M. Lieber. Rational growth of branched and hyperbranched nanowire structures. *Nano Letters*, 4(5):871--874, May 2004.

[42] H. Wang, L. A. Zepeda-Ruiz, G. H. Gilmer, and M. Upmanyu. Atomistics of vapour–liquid–solid nanowire growth. *Nature Communications*, 4, June 2013.

[43] H. Yan, H. S. Choe, S. Nam, Y. Hu, S. Das, J. F. Klemic, J. C. Ellenbogen, and C. M. Lieber. Programmable nanowire circuits for nanoprocessors. *Nature*, 470(7333):240--244, 2011.

[44] C.-Y. Yeh, Z. Lu, S. Froyen, and A. Zunger. Zinc-blende–wurtzite polytypism in semiconductors. *Physical Review B*, 46(16):10086--10097, Oct. 1992.

[45] H. Zheng, J. Wang, J. Y. Huang, J. Wang, Z. Zhang, and S. X. Mao. Dynamic Process of Phase Transition from Wurtzite to Zinc Blende Structure in InAs Nanowires. *Nano Letters*, 13(12):6023--6027, Dec. 2013.


SIGILLVM VNIVERSITATIS HAFNIENSIS
1479 FVNDATÆ
REFORMATÆ 1537